

UNCLASSIFIED

AD NUMBER
ADB193102
NEW LIMITATION CHANGE
TO Approved for public release, distribution unlimited
FROM Distribution authorized to U.S. Gov't. agencies and their contractors; Administrative/Operational Use; DEC 1959. Other requests shall be referred to National Aeronautics and Space Administration, Washington, DC.
AUTHORITY
NASA TR Server website

THIS PAGE IS UNCLASSIFIED



AD-B193 102



THE UNIVERSITY OF MICHIGAN

COLLEGE OF ENGINEERING

DEPARTMENT OF AERONAUTICAL AND ASTRONAUTICAL ENGINEERING

COPY 1

Final Report

Upper-Atmosphere Structure Measurements

APR 5 1960

[REDACTED] SA
CLEVELAND, OHIO

DTIC
ELECTE
AUG 09 1994
S G D

74P

94-24820



Under Contract With:

National Aeronautics and Space Administration

Contract No. NASw-4

Washington, D.C.

94 8 05 001

Administered by:

December 1959

THE UNIVERSITY OF MICHIGAN RESEARCH INSTITUTE • ANN ARBOR

CN-81250

31250

THE UNIVERSITY OF MICHIGAN
COLLEGE OF ENGINEERING
Department of Aeronautical and Astronautical Engineering

Final Report

UPPER-ATMOSPHERE STRUCTURE MEASUREMENTS

Submitted for the project by

E. J. Schaefer

UMRI Project 2841

under contract with:

NATIONAL AERONAUTICS AND SPACE ADMINISTRATION
CONTRACT NO. NASw-4
WASHINGTON, D.C.

administered by:

THE UNIVERSITY OF MICHIGAN RESEARCH INSTITUTE ANN ARBOR

December 1959

Accession For	
NTIS CRA&I	<input type="checkbox"/>
DTIC TAB	<input checked="" type="checkbox"/>
Unannounced	<input type="checkbox"/>
Justification	
By	
Distribution /	
Availability Codes	
Dist	Avail and/or Special
12	

THE UNIVERSITY OF MICHIGAN PROJECT PERSONNEL

(Both Full-Time and Part-Time)

Bartman, Frederick, L., M.S., Research Engineer
Brown, John, M.S., Associate Research Engineer
Glass, David Roger, M.S.E. (AeE), Research Engineer
Gleason, Kermit L., Instrument Maker
Harrison, Lillian M., Secretary
Henry, Harold F., Electronic Technician
Jones, Leslie M., B.S., Project Director
Loh, Leslie, M.S., Associate Research Engineer
Mosakewicz, Mary C., Secretary
Nichols, Myron H., Ph.D., Professor of Aeronautical and Astronautical Engineering
Pattinson, Theodore R., Electronic Technician
Perkins, Ronald J., Assistant in Research
Samborski, Cassimere, Instrument Maker
Schaefer, Edward J., M.S., Principal Investigator
Schumacher, Robert, B.S. (EE), Assistant in Research
Thornton, Charles, Assistant in Research
Wenk, Norman, J., B.S., Research Engineer
Wenzel, Elton A., Research Associate

TABLE OF CONTENTS

	<u>Page</u>
LIST OF TABLES	vii
LIST OF FIGURES	ix
SUMMARY	xi
PURPOSE	xi
1. INTRODUCTION	1
2. BACKGROUND	3
3. APPROACH	7
4. MASSENFILTER	9
4.1. Principle of Operation	9
4.2. Design Equations	12
4.3. Design and Description of Laboratory Massenfilter	15
4.4. Massenfilter Test Results	17
4.4.1. Tests of Initial Design	21
4.4.2. Variation of Design Parameters	23
4.5. Flight Model Design	30
4.5.1. Ionization Volume	30
4.5.2. Electron Source	32
4.6. Advantages	32
5. OMEGATRON	35
5.1. Principle of Operation	35
5.2. Design and Preliminary Test	35
5.3. Tests of Final Model	42
5.4. Conclusions	49
6. INSTRUMENTATION PACKAGE	51
7. ELECTRONIC CIRCUITRY	53
7.1. Massenfilter Driving Oscillator and Rectifier	53
7.2. Emission Regulator	53
7.3. Telemetry	57
8. VACUUM EQUIPMENT	59
9. FUTURE PROGRAM	63
10. ACKNOWLEDGMENTS	65
APPENDIX. OMEGATRON: PRINCIPLE OF OPERATION	67
REFERENCES	73

LIST OF TABLES

<u>Table</u>	<u>Page</u>
I. Structural Parameters of the Atmosphere	7
II. Initial Design Parameters	16
III. Inlet Port Configurations	26
IV. Omegatron Working Parameters	35
V. Comparison of Experimental and Predicted Resolutions	42
VI. Comparison of Experimental and Predicted Resolutions	47
VII. Effect of Initial Velocity	70

LIST OF FIGURES

<u>Fig.</u>	<u>Page</u>
1. Satellite densities as a function of altitude compared with ARDC densities.	4
2. Mean molecular weight as a function of altitude.	5
3. Massenfilter cylindrical electrode arrangement.	9
4. Massenfilter stability diagram.	11
5. Massenfilter schematic.	16
6. Massenfilter exploded view.	18
7. Massenfilter partially assembled.	19
8. Assembled massenfilter.	20
9. Massenfilter spectrograms: resolution as a function of U/V_{RMS} .	22
10. Massenfilter composite N_2 spectrograms: resolution and peak shape as functions of U/V_{RMS} .	22
11. Massenfilter N_2 spectrograms: resolution and peak shape as functions of V_{in} .	24
12. Massenfilter composite N_2 spectrograms: resolution and peak shape as functions of V_{in} .	24
13. Massenfilter resolutions as functions of V_{in} .	25
14. Massenfilter spectrograms: abundances of Ne^{20} and Ne^{22} .	25
15. Massenfilter resolution and peak ion current as functions of U/V_{RMS} .	27
16. Massenfilter resolution as a function of inlet port configuration.	28
17. Massenfilter ion current as a function of inlet port configuration.	29
18. Laboratory cylindrical lens components.	31
19. Omegatron schematic.	37

LIST OF FIGURES (Concluded)

<u>Fig.</u>	<u>Page</u>
20. Open-box omegatron.	38
21. Open-box omegatron closeup.	38
22. Open-box omegatron spectrum.	39
23. Enclosed omegatron.	40
24. Commercial omegatron.	40
25. Helium peak, commercial omegatron.	41
26. Ne, N ₂ , and A spectrum, commercial omegatron.	41
27. Peak argon ion current as a function of E ₀ .	44
28. Peak ion currents as functions of E ₀ at various trapping voltages.	45
29. Enclosed omegatron He peak.	46
30. Enclosed omegatron spectrum of Ne, A, and their isotopes.	46
31. Omegatron resolution of Ne as a function of E ₀ .	48
32. Data cylinder separation.	52
33. Massenfilter oscillator and rectifier.	54
34. Circuit diagram: massenfilter oscillator and rectifier.	54
35. Laboratory test setup.	55
36. Circuit diagram: emission regulator.	56
37. Emission regulator.	56
38. Glass vacuum system.	60
39. Portable glass vacuum system.	60
40. Closeup of glass vacuum system.	61
41. Stainless-steel vacuum system.	62
42. Omegatron field coordinates.	67

SUMMARY

The theory of operation of, and the experimental results obtained from, two types of mass spectrometer, the massenfilter and the omegatron, are presented. It is concluded that the massenfilter exhibits some significant advantages over the omegatron as well as other types of mass spectrometers previously used in upper-atmosphere research. At comparable resolutions, these advantages include simplicity of construction, ability to operate to higher densities, and operation which is relatively independent of ionic energies. This latter leads to spectra uniquely related to the gas under analysis and interpretation of results is simplified. Elimination of the magnetic field reduces weight as compared with the omegatron and conventional spectrometers. Obtainable sensitivity in terms of ion current per unit pressure and unit electron beam current should be comparable to the Bennett tube.

Inasmuch as one of the objectives is to measure the extent of dissociation in the ambient atmosphere, it is necessary to eliminate collision processes with the apparatus in which recombination is likely to occur. A preliminary ion source design for the massenfilter is described in which this probability is reduced to an acceptable value.

A separable instrument package, designed to avoid outgassing and recombination problems, is described.

PURPOSE

The purpose of the research as set forth in the contract is to conduct a "special investigation for development of rocket instrumentation packages for measuring the properties of the upper atmosphere." By mutual agreement with NASA scientists, this broad objective has been more specifically defined to develop instrumentation capable of yielding pressure, temperature, density, and composition data in the range of from 100-200 kilometers. It is further understood that:

- a. Composition measurements in sufficient detail to yield mean molecular weight are required, the details of dissociation of oxygen and nitrogen are highly desirable, and the relative abundance of the minor constituents need not be an initial objective.
- b. Synoptic capability is a primary objective.

1. INTRODUCTION

This report summarizes the progress of the upper-atmosphere research project carried out by the Department of Aeronautical and Astronautical Engineering of The University of Michigan in fulfillment of National Aeronautical and Space Administration Contract No. NASw-4 with The University of Michigan Research Institute. The first-year contract period was 27 October 1958 to 1 November 1959. The contract was executed about 1 December 1958 at which time technical work began. This report presents new material as well as materials covered in a memorandum report of June, 1959, and letter reports transmitted 3 September 1959 and 23 October 1959.

2. BACKGROUND

As a result of rocket measurements made since 1946 and particularly during the IGY aboard a variety of rockets, the physical structure of the atmosphere—pressure, temperature, density, and composition—is generally known to an altitude of 90 km. Synoptic variations and a few special phenomena related to structure, such as ozone and wind systems, are not as well known. However, it is generally agreed that satisfactory techniques for obtaining more synoptic data are available. Many organizations have gathered such data and the High Altitude Engineering Laboratory in the Department of Aeronautical and Astronautical Engineering of The University of Michigan has been a significant contributor.

Above 90 km, however, the situation is far different. The mean free path becomes the same order of magnitude as the dimensions of the rocket-borne instruments. Measurements of the structural parameters based on aerodynamic flow theory become subject to large error or become completely unworkable. Drag cannot be measured with present techniques except by integration of long-term effects, acoustical energy cannot be coupled to the atmosphere, and out-gassing of the instruments and vehicle can easily overwhelm the parameters under investigation. In addition, dissociation of oxygen and nitrogen—which makes composition measurement so important—often introduces large errors in these measurements due to recombination.

Until the advent of satellites, virtually no measurements of densities in the region 200 km and beyond existed. Several points were obtained by satellites and are compared in Fig. 1 with densities obtained from the ARDC Model Atmosphere, 1956.¹ The measured values at 200 km are seen to exceed those theoretically obtained by nearly a factor of 10 and the discrepancy increases with altitude. Further use of density data to derive pressures and temperatures requires a knowledge of mean molecular weights. Figure 2 illustrates the wide discrepancy in these values obtained from the ARDC Model Atmosphere, from Whitney's Model² based on the theories of Chapman³ and Nicolet,⁴ and from measurements taken by NRL.⁵ It is to be expected, of course, that some of the variations are real. Nevertheless, the need for more and independent data in an effort to resolve the ambiguities is self-evident. The research sponsored under this contract is directed toward contributing data in these areas.

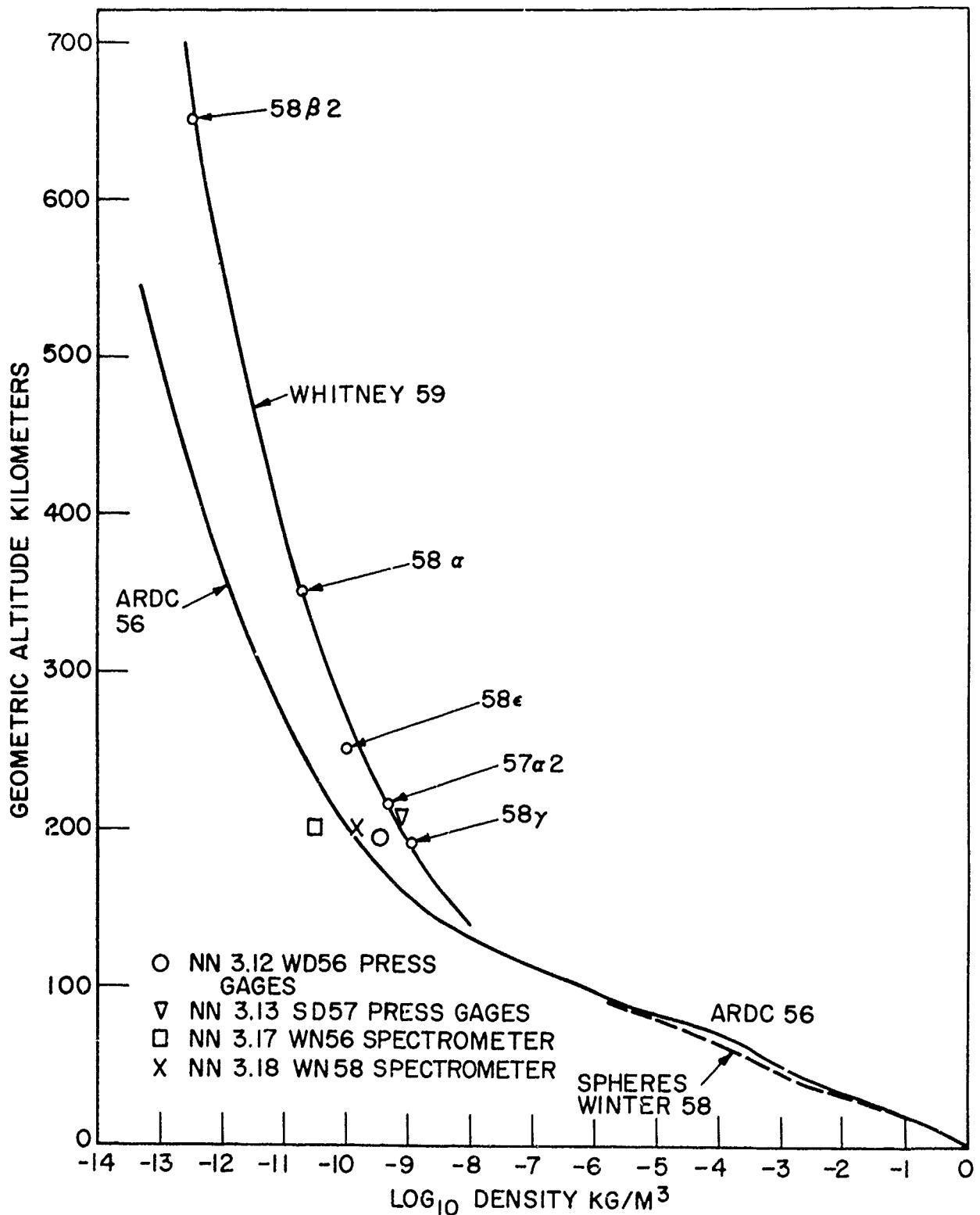


Fig. 1. Satellite densities as a function of altitude compared with ARDC densities. Also shown are some vertical rocket points obtained by various methods. W (winter, S (summer), D (day), N (night).

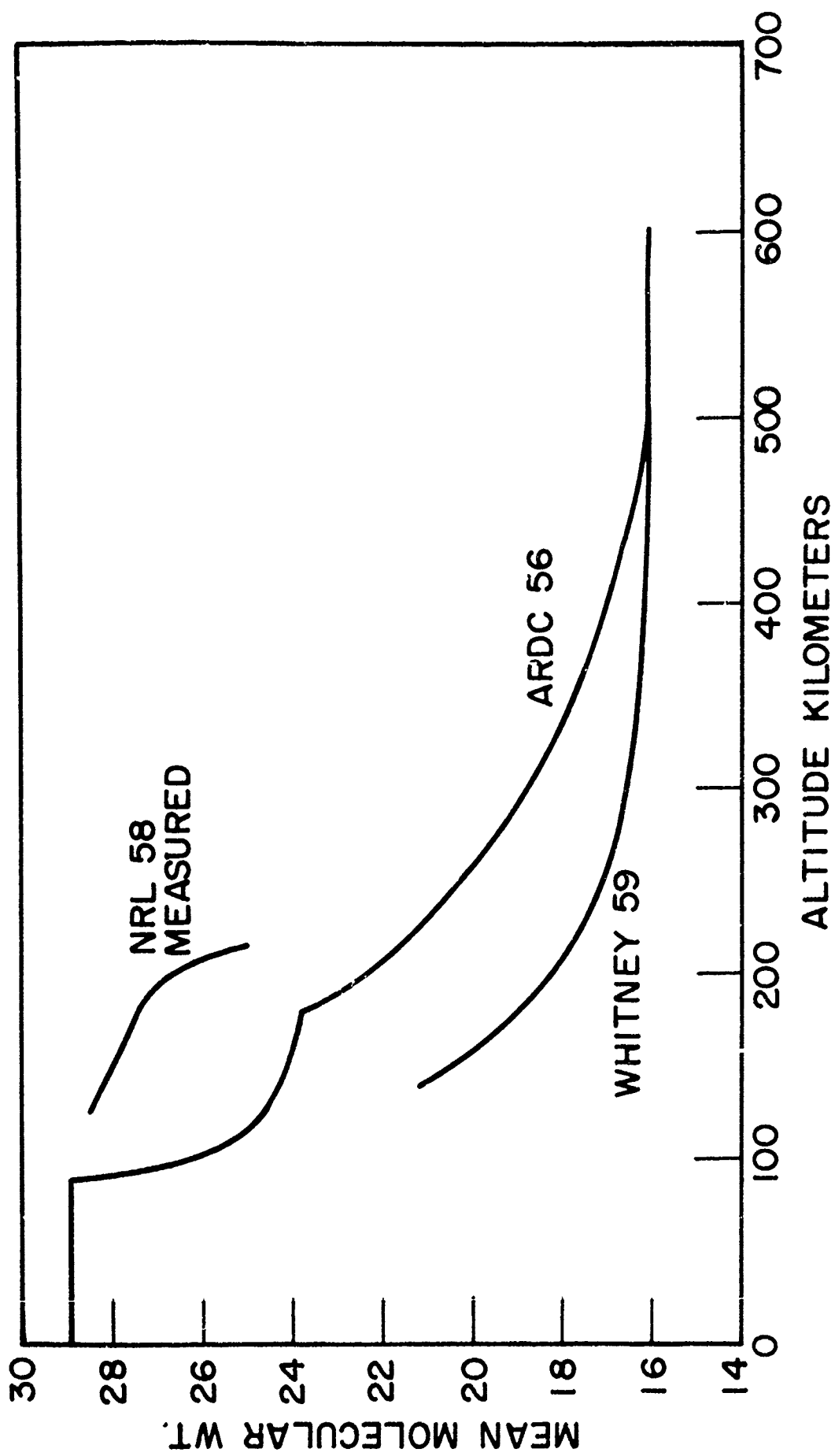


Fig. 2. Mean molecular weight as a function of altitude.

3. APPROACH

The four parameters of interest in this investigation, P, T, ρ , and M, are independently related by the equation of state and by the hydrostatic equation. Measurement of any two, therefore, is sufficient to calculate the remaining unknowns. The early effort of the project was directed toward a selection of the parameters to measure and the basic methods by which to perform these measurements. The anticipated range of these parameters and of others closely related was obtained from Ref. 1 as follows:

TABLE I
STRUCTURAL PARAMETERS OF THE ATMOSPHERE

	<u>0 km</u>	<u>100 km</u>	<u>200 km</u>
Pressure (mm Hg)	760	3.46×10^{-4}	2.20×10^{-7}
Density (kg/m ³)	1.225	7.12×10^{-7}	1.11×10^{-10}
Temperature (°K)	288.16	207	712
Mean molecular weight	28.966	26.48	22.36
Mean free path (cm)	6.63×10^{-8}	10.43	5.65×10^4
Number density (no./m ³)	2.55×10^{25}	1.62×10^{19}	2.99×10^{15}
Average particle speed (m/sec)	458.9	407	821

Various methods of measuring pressure, mass density, temperature, mean molecular weight, and number density were considered. In the range of values given by Table I, it was concluded that measurements of the number of molecules per unit volume (hereafter called particle density) using an ionization gage and measurement of composition by in-flight mass spectrometry was the best approach. These two sets of data will yield mean molecular weight and mass density from which temperature and pressure can be calculated.

Several instruments capable of in-flight mass spectrometry were considered. Included were the diatron (similar in principle to the conventional mass spectrometer), the Bennett and Bendix time-of-flight mass spectrometers, the omegatron, and, at a later date, the Paul Massenfilter. Of these, the Paul Massenfilter has been selected as the instrument most adaptable to the requirements of the contract.

4. MASSENFILTER

4.1. PRINCIPLE OF OPERATION

The massenfilter, described by Paul et al.,⁶ separates ions by exposing them to an electric field which is a linear function of the coordinates. The potential of such a field is expressible in the form,

$$V_{x,y,z} = V_0 (ax^2 + by^2 + cz^2) \quad (4.1.1)$$

where $a + b + c = 0$ since the Laplacian of a field in charge-free space must vanish. In the massenfilter design, Paul sets $a = -b = 1/R_0^2$, $c = 0$. Such a field is produced exactly by hyperbolic electrodes arranged 90° apart. A close approximation out to $R = 0.8 R_0$ ⁷ is provided by cylindrical electrodes (Fig. 3) when $R_{rod}/R_0 = 1.16$ and the operating voltages are given by

$$V_{0x} = U + V \cos \omega t \quad (4.1.2)$$

$$V_{0y} = -V_{0x} \quad (4.1.3)$$

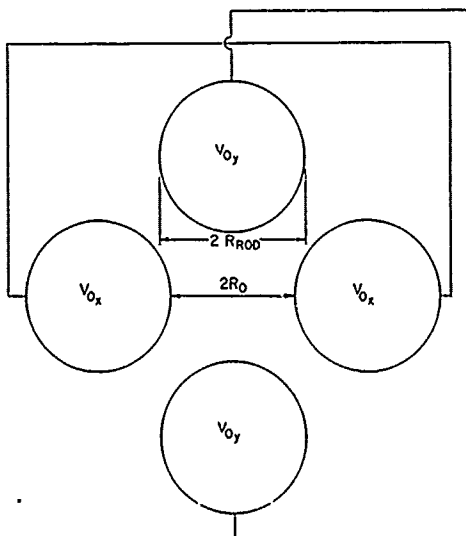


Fig. 3. Circular electrode arrangement.

The potential at any point of the field is given by

$$V_{x,y} = (U + V \cos \omega t) \frac{(x^2 - y^2)}{R_0^2} \quad (4.1.4)$$

and the equations of motion of a singly charged ion are

$$m\ddot{x} + 2e (U + V \cos \omega t) \frac{x}{R_0^2} = 0 \quad (4.1.5)$$

$$m\ddot{y} - 2e (U + V \cos \omega t) \frac{y}{R_0^2} = 0 \quad (4.1.6)$$

$$m\ddot{z} = 0 \quad (4.1.7)$$

Equation (4.1.7) merely indicates the z-component of velocity is constant. Substitution of the relations

$$\omega t = 2\xi \quad (4.1.8)$$

$$a = \frac{8eU}{mR_0^2 \omega^2} \quad (4.1.9)$$

$$q = \frac{4eV}{mR_0^2 \omega^2} \quad (4.1.10)$$

transforms Eqs. (4.1.5) and (4.1.6) to

$$\frac{d^2x}{d\xi^2} + (a + 2q \cos 2\xi)x = 0 \quad (4.1.11)$$

$$\frac{d^2y}{d\xi^2} - (a + 2q \cos 2\xi)y = 0 \quad (4.1.12)$$

Both of these equations are Mathieu differential equations. The solution of either of these yields a complicated a-q plot of stability regions.^{6,8} Within these regions x (or y) remain bounded as $\xi \rightarrow \infty$ while outside these regions, x (or y) $\rightarrow \infty$ as $\xi \rightarrow \infty$. For an ion to be stable, both the x and y components of motion must remain bounded. Hence both working points a_x, q_x and a_y, q_y [$= -a_x, -q_x$ from Eqs. (4.1.11) and (4.1.12)] must lie in stable regions. Reflecting the stability diagram about the q-axis results in the composite stability diagram of Ref. 6 (Fig. 4) wherein both conditions for stability are met simultaneously. In addition to the region illustrated in Fig. 4, another small region exists at high values of a and q and at a high value of a/q. This small region has not been investigated since it leads to impractically large voltages for the heavy gases. It may, however, be quite useful for the analysis of hydrogen and helium in other applications.

For fixed values of $R_0, \omega, U,$ and $V,$ (4.1.9) and (4.1.10) show that the work point of an ion is determined only by $m/e.$ Since the ratio $a/q = 2 U/V$ is independent of mass, all ions lie on a line through the origin, the slope of which is given by $2 U/V.$ For values of $a/q < 0.237/0.706 = 0.336,$ this line intersects

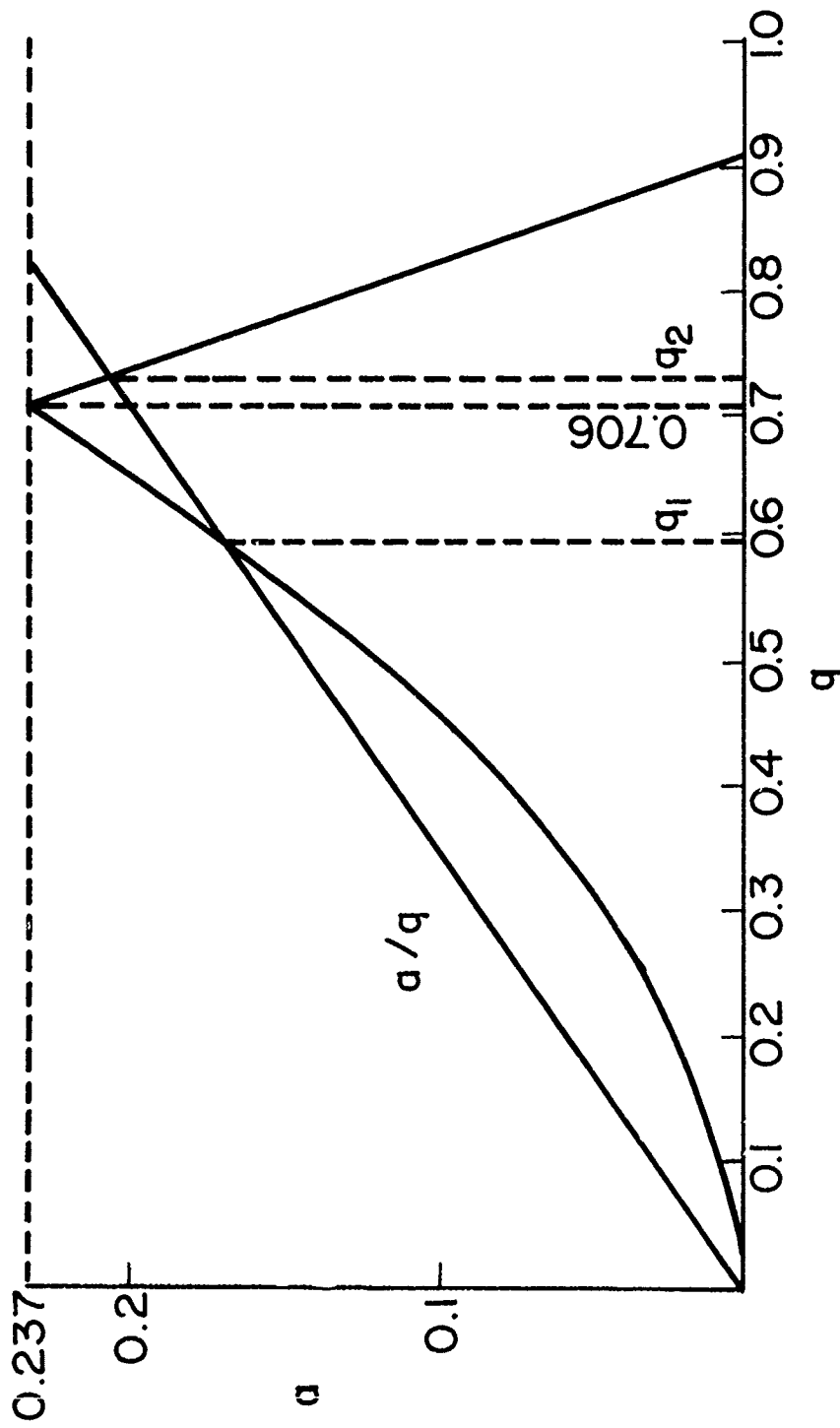


Fig. 4. Massenfilter stability diagram.

the triangle of Fig. 4. Only those ions whose work point lies between the intercept points (q_1q_2) are stable. By increasing $2 U/V$, the intercepts can be moved toward the apex of the triangle and the intercept range can be made as narrow as desired until the line no longer intersects the triangle and nothing is stable. It will be shown later that experimental determination of this marginal ratio agrees with the theoretical prediction within the limits of observational accuracy.

Not only must an ion be stable by the definitions given above (i.e., x and y are bounded as $\xi \rightarrow \infty$), but its amplitude of oscillation must remain smaller than R_0 so that it can reach the collector without first impinging on one of the rods. As resolution is increased, we move closer to the apex of the stability diagram (Fig. 4) and any work point within lies closer to the stability boundaries. Thus the maximum excursion amplitude of an ion grows with resolution, other factors remaining the same. The maximum excursion amplitudes depend also on the initial injection conditions, $x_0, y_0, \dot{x}_0, \dot{y}_0$, and ωt_0 . As the working point moves into the stable region, an increase of collector ion current with distance from the nearest stability limit occurs since ions which enter farther off the axis progressively reach the collector. As the second stability limit is approached, the ion current decreases. To achieve 100% transmission of the stable ions somewhere between the stability intercepts, the initial conditions must be limited. Such limitation obviously becomes more severe as the resolution is increased. This gives rise to two possible modes of operation:

- a. Low resolving power in which the spectral peaks appear as trapezoids with a flat top and 100% transmission. Amplitude is independent of resolving power.
- b. High resolution in which the peaks approach triangles and their amplitude becomes inversely proportional to resolving power.

4.2. DESIGN EQUATIONS

In the case of the massenfilter, resolution is defined as the ratio $m/\Delta m$ ($= -q/\Delta q$) where Δm is taken at half-amplitude. For 100% transmission and low resolution, base width and half-amplitude width are nearly the same due to the flat-top and steep sides. By geometric construction near the apex of the stability diagram of Fig. 4, Paul shows that

$$\left(\frac{m}{\Delta m}\right)_{100\%} = \frac{0.178}{0.237 - a_{0.706}} \quad (4.2.1)$$

where $a_{0.706}$ is the ordinate of the working point when $q = 0.706$. For high resolution, where the peaks are nearly triangular, the value of Δm at half-amplitude is approximately half that at the base and, by the foregoing definition, the resolution is twice that given by Eq. (4.2.1). Paul further shows that, for injection parallel to the axis, the optimum inlet port diameter is

given approximately by

$$D_{in} = \frac{R_0}{\sqrt{m/\Delta m}} \quad (4.2.2)$$

At this value of inlet port diameter, 100% transmission should just be realized when the work point is equidistant from the stability limits (Fig. 4). In addition, for those ions injected on the axis, it is shown that the maximum permissible radial velocity for a stable ion is given by

$$\dot{x}_{Omax}, \dot{y}_{Omax} = 0.16 R_0 \omega \sqrt{\Delta m/m} \quad (4.2.3)$$

It should be noted that Eqs. (4.2.2) and (4.2.3) are mutually exclusive, i.e., for an inlet port diameter given by Eq. (4.2.2), the value of Eq. (4.2.3) must be zero and vice versa. Hence, if an inlet port is designed according to the criteria given by these equations, the realizable resolution of the massfilter will be somewhat less than the design value. Further, the resolution used in these equations, and in those to follow, is based on the width of the peak at half amplitude and, for the triangular peaks obtained up to 100% transmission, is therefore twice the value given by Eq. (4.2.1).

To be excited to an amplitude greater than R_0 , an unstable ion must reside within the four-pole field for a minimum number of cycles, n , of the driving frequency. The number of cycles is dependent on the resolving power. This number has been experimentally determined around a resolution of 100 and is given by Paul as approximately

$$n = 3.5 \sqrt{m/\Delta m} \quad (4.2.4)$$

Based on Eq. (4.2.4), one can determine the maximum ion injection velocity. From the apex coordinates of the stability diagram of Fig. 4 where $a = 0.237$ and $q = 0.706$ and from Eqs. (4.1.9) and (4.1.10), after conversion to practical units, it follows that

$$V = 7.22 A f^2 R_0^2 \text{ volts peak} \quad (4.2.5)$$

where

- A = atomic mass number,
- f = frequency in megacycles, and
- R_0 = field radius in cm.

Also

$$\frac{a}{q} = \frac{0.237}{0.706} = 0.336 = \frac{2U}{V} \quad (4.2.6)$$

Hence

$$U = 0.168V = 1.21 Af^2 R_0^2 \text{ volts} \quad (4.2.7)$$

Using Eq. (4.2.3) and substituting from Eq. (4.2.5), the maximum permissible radial energy for focusing of stable ions injected on the axis is given approximately by

$$W_R = \frac{V}{15 (m/\Delta m)} \text{ electron volts} \quad (4.2.8)$$

Using Eq. (4.2.4), it can be shown that the maximum voltage through which the ions can be accelerated prior to injection into the field is

$$V_{in_{max}} = 0.042 A L^2 f^2 \frac{\Delta m}{m} \text{ volts} \quad (4.2.9)$$

where

L = length of four-pole field in cm, and
f = driving frequency in megacycles.

An accelerating voltage greater than $V_{in_{max}}$ as given by Eq. (4.2.9) will result in a shorter residence time than required to undergo the number of cycles given by Eq. (4.2.4). Hence, under these conditions, all unstable ions will not be excited to an amplitude equal to or greater than R_0 with resultant decrease in effective resolution.

Because of the field-free space therein, ion paths through the injection port are straight lines. From the foregoing, it should be designed to limit the maximum ion exit angle. The value of this angle can be shown to be

$$\tan \theta = \frac{v_R}{v_{in}} = \sqrt{\frac{W_R}{W_{in}}} = \sqrt{\frac{W_R}{V_{in}}} \quad (4.2.10)$$

where

v_R = radial velocity,
 v_{in} = axial velocity, and
 W_R is obtained from Eq. (4.2.8) and V_{in} from Eq. (4.2.9).

From Eqs. (4.2.5) and (4.2.6), one can see that a mass sweep can be realized by sweeping either frequency or voltage, maintaining the ratio of U/V constant. Since a voltage sweep is simpler to obtain and yields a linear mass scale for a linear voltage sweep, this has been the method selected in all subsequent work.

Finally, except for changes in charge which might be experienced, the tendency of an ion to be stable or unstable is not changed to a first approximation

by small-angle scattering due to collision with residual gas molecules. Thus, the massenfilter can reasonably be expected to operate up to relatively high pressures. In Ref. 6, Paul illustrates the CH_3 peaks obtained at pressures of 8.5×10^{-5} mm Hg and 6.5×10^{-4} mm Hg. No significant change in shape can be seen in an apparatus in which the total length of ion path between creation and collection was approximately 160 cm, approximately ten times the length of the flight design to be described.

4.3. DESIGN AND DESCRIPTION OF LABORATORY MASSENFILTER

Since resolution as defined in the previous section refers to the half-amplitude width of the peak, a design value of 40 was chosen. This corresponds to an equivalent value of 20 at the base of the triangular peak theoretically obtained when resolution is at the limiting value for 100% transmission. In addition, this value provides for a small adjustment to achieve 100% transmission for those ions simultaneously at the maximum values of both Eqs. (4.2.2) and (4.2.3). The maximum peak a-c voltage was arbitrarily selected at 500 volts (for mass 46) and the rod length was selected at 12.75 cm (5 in.). In addition, the ion injection voltage was selected at 45 volts to avoid difficulties involved with controlling low-energy ion trajectories and still keep the driving frequency as low as possible. Substituting the selected values of injection voltage, length, and resolution into Eq. (4.2.9), we find, for mass 46, an operating frequency of 2.39 Mc. Using Eq. (4.2.5), an R_0 of 0.512 cm is obtained. In Section 4.1 it was noted that a ratio $R_{\text{rod}}/R_0 = 1.16$ yielded the closest approximation to the ideal hyperbolic field. Thus R_{rod} is 0.595 cm. Equation (4.2.8) yields a maximum permissible radial energy of 0.833 electron volts and Eq. (4.2.10) shows $\tan \theta = 0.136$ or $\theta = 7.75^\circ$. As partial compensation for finite dimension of the inlet port, the initial design limited the injection angle to about 5.25° . Finally, Eq. (4.2.2) gives an injection port diameter of 0.081 cm (0.032 in.). The initial design parameters are grouped below in Table II.

The following comments on this design may be made, based on the foregoing discussion. First, since the intercept range on the stability diagram is independent of mass, the ultimate resolution based on this consideration is constant for all gases. Secondly, the combination of L , V_{in} , and f were obtained for a mass number of 46. Lower masses will therefore spend less time and a fewer number of rf cycles within the field. Hence one must operate further from the stability limit to remove all unstable ions. The practical effect is to reduce the effective resolution of the lighter masses somewhat. However, this effect should be acceptable since lower resolution of the lighter masses is tolerable. Finally, because injected ions can have both an initial radial component of velocity and an initial displacement off the axis, the intercept range on the stability diagram may have to be increased slightly above design values to achieve 100% transmission.

A laboratory massenfilter designed according to the parameters of Table II was constructed and is shown schematically in Fig. 5. Two tungsten filaments, connected in parallel, are used as the electron source. In typical operation at

TABLE II
INITIAL DESIGN PARAMETERS

Quantity	Symbol	Value
Mass number	A	46
Resolution	$m/\Delta m$	40
Peak driving voltage	V	500 volts
Length of field	L	12.75 cm
Ion injection voltage	V_{in}	45 volts
Frequency	f	2.39 Mc
Field radius	R_o	0.512 cm
Rod radius	R_{rod}	0.595 cm
Number of cycles	n	22
Maximum radial energy	W_R	0.833 electron volt
Maximum injection angle	θ	7.75° (5.25° used)
Injection port diameter	D_{in}	0.081 cm (0.032 in.)

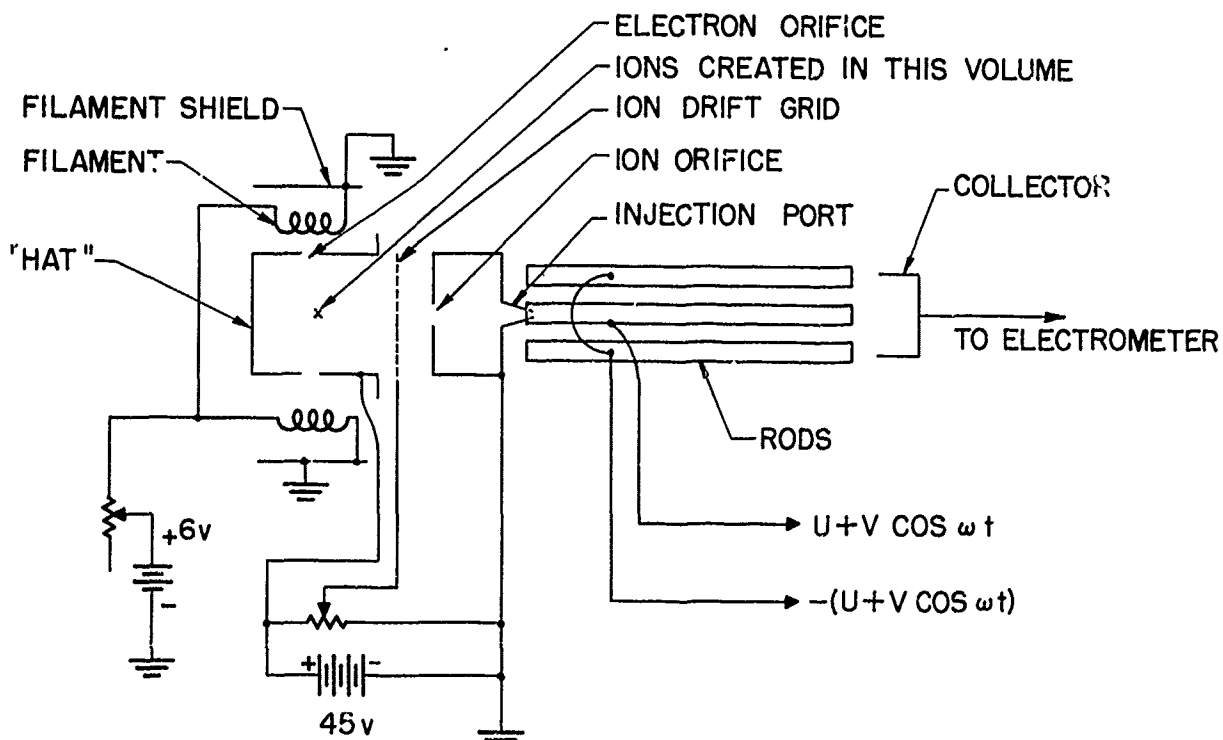


Fig. 5. Massenfilter schematic.

6 volts, the total filament current is 3 amperes and the total emission current is between 2 and 3 milliamperes. Electrons are accelerated toward the orifices in the "hat" structure which surrounds the ionizing volume by virtue of the fields created by the battery in Fig. 5 which is typically 45 volts. This appears to be a reasonable compromise between peak ionization efficiency and a low enough electron energy to keep double ionization negligible. The same battery produces the ion accelerating fields.

The shields behind the filaments help direct the emitted electrons toward the "hat." Those electrons which pass through the orifices are available to ionize gas within the volume. The ions which are created experience a force toward the drift grid by virtue of the negative field gradient supplied by that grid. The design purpose of the drift grid is to keep the fields inside the "hat" low and to restrict the greatest accelerating fields to the region between the inlet orifice and drift grid. In this way, it was hoped to approach a monoenergetic beam irrespective of the point within the "hat" at which the ion was created. In practice, it did not seem to matter much and, in most runs to be described, the drift grid was set for maximum ion current. This occurred at some setting slightly above ground potential, presumably due not only to the stronger fields to pull the ions from the "hat" volume, but also to the focusing action of the fields. The purpose of the orifice is to provide a field-free space near the injection port so no further deflection of the ion path can occur. The injection port admits only those ions conforming to the initial conditions previously described. Upon negotiating the four-pole field formed by the rods, stable ions reach the collector and the transferred charge is the current input to the electrometer.

Figures 6-8 are photographs of the test model of the massenfilter. Figure 6 shows the massenfilter in exploded form. The separately assembled rod structure and ion source structure are shown in Fig. 7. Here the hinged filament shield is easily seen in the open position to allow the filament to be welded into place. The completed massenfilter and collector structures ready for insertion into the vacuum housing are shown in Fig. 8.

4.4. MASSENFILTER TEST RESULTS

As seen in Section 4.3, adaptation of the massenfilter to high-altitude research required several compromises in the various design parameters, such as overall size, operating voltages, etc. Consequently, the preliminary tests on the laboratory model of the massenfilter were made for the purpose of comparing actual performance characteristics with those predicted by the design equations. Following this, specific changes in the design parameters—chiefly the inlet conditions as determined by the injection port—were made to determine their effects on the massenfilter performance. Throughout what follows, resolution is defined on the basis of peak width at half-amplitude unless otherwise stated. The point at which 100% transmission is lost is determined when the height of a given peak begins to decrease with increasing a/q ratio. In practice, comparisons of res-

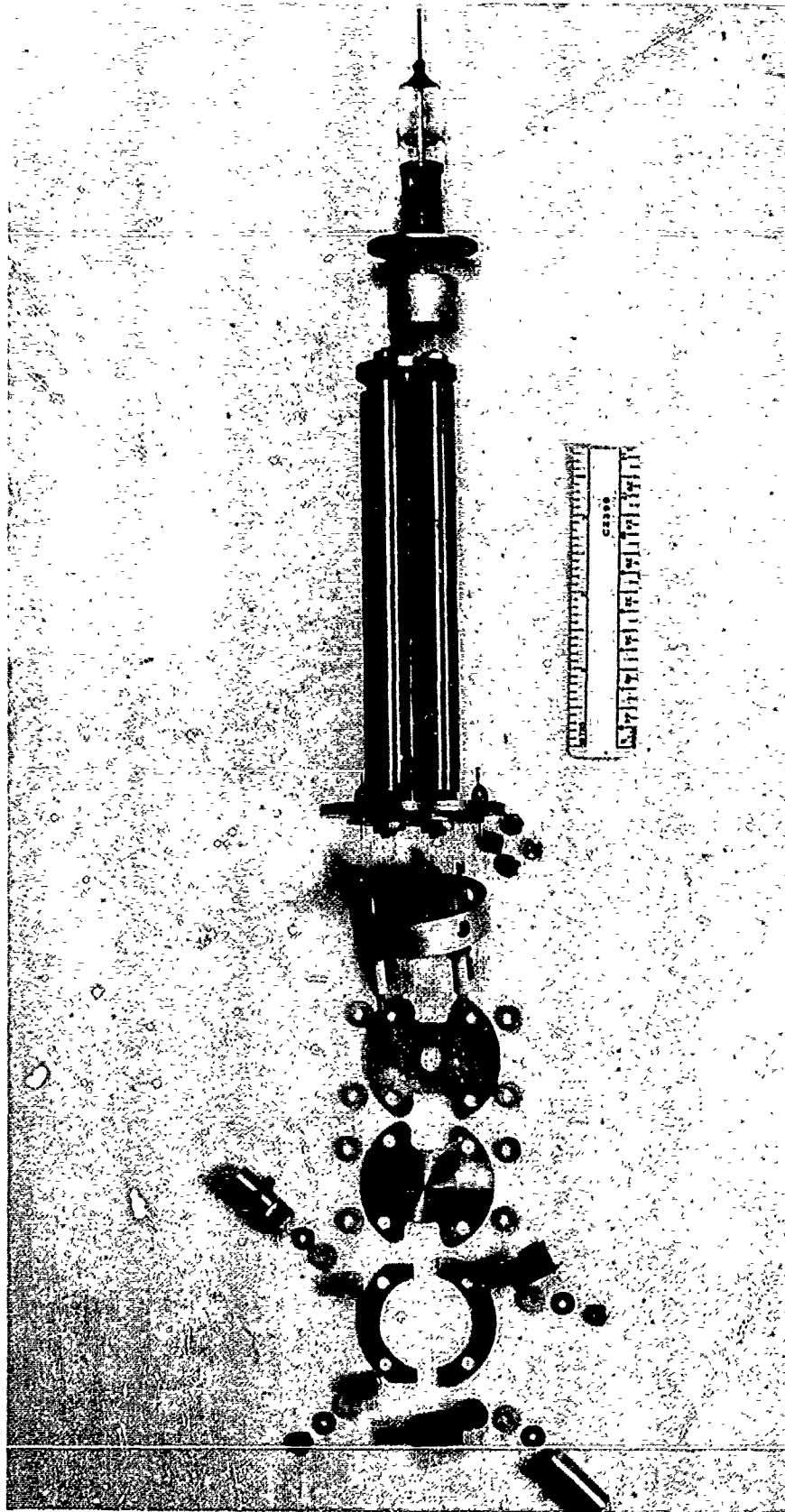


Fig. 6. Massenfilter exploded view.



Fig. 7. Massenfilter partially assembled.

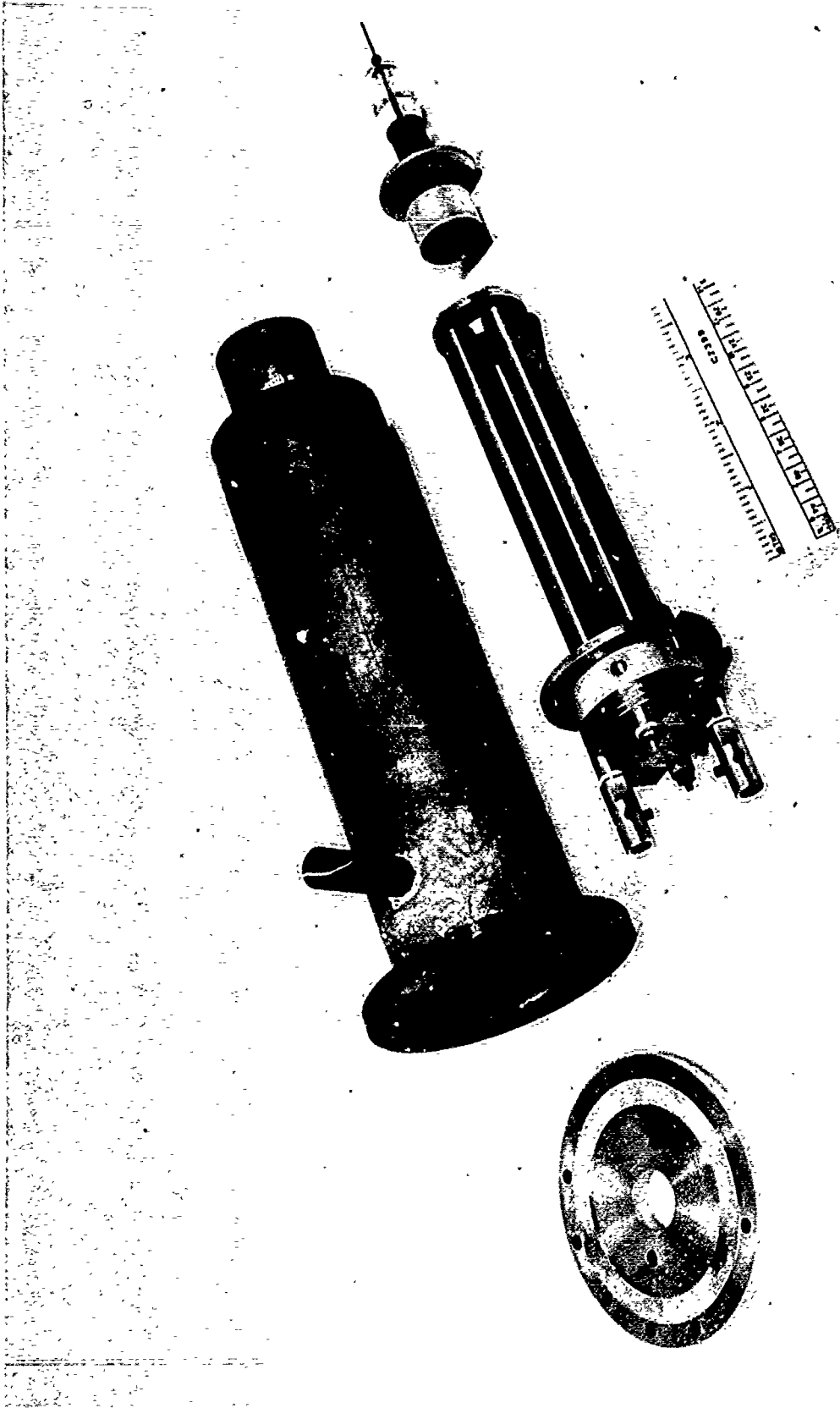


Fig. 8. Assembled massenfilter.

olution were made at the 95% transmission point for a given species since this point could be more precisely determined. The criteria of greatest interest is the best resolution obtainable without significant loss of transmission and the maximum current obtainable under conditions of 100% transmission and acceptable resolution.

4.4.1. Tests of Initial Design.—In Section 4.1, the ratio of coordinates of the apex of the triangular stability region was given as 0.336 which is equal to $2 U/V$. Thus U/V is 0.168. Since most meters are calibrated in RMS values, the ratio of $U/V_{RMS} = 0.238$ is more convenient to work with in laboratory practice.

By the theory presented in Section 5.1 we note that, as the ratio of U/V_{RMS} starts at a low value and approaches 0.238, the peaks should become narrower since the stability region determined by the intercept range becomes smaller. At some point just prior to reaching 0.238, the side slopes of the peak should merge into a triangle and the peak value should decrease since 100% transmission is no longer taking place. Finally, beyond U/V_{RMS} of 0.238, the mass line no longer intercepts the stability triangle, nothing is stable, and no transmission occurs. Figure 9 illustrates this behavior in the design massfilter in a series of spectrograms in which U/V_{RMS} is increased from 0.20 to 0.24 in five steps. The right-hand peak is nitrogen ($AMU = 28$). The left-hand peak is an unidentified residual gas of approximately mass 17 (possibly OH or CH_4) which appears whenever a new model is first turned on and then gradually disappears with operation and pumping. It will be noted that both peaks disappear completely at $U/V_{RMS} = 0.24$. It will also be noted that, as U/V_{RMS} is increased, the left-hand slope, corresponding to lower mass numbers, moves to a much greater extent than the right-hand slope. This behavior follows directly from Fig. 4 and the respective angles at which the mass line crosses the stability limits. The increase at the far left (corresponding to zero mass number), is the transmission of all ions down the field since the rod voltages are zero. Although tests have not yet been run to verify the assumption, the collector current at this point should be a measure of overall particle density. In this manner, it is anticipated that one instrument can be calibrated to yield particle density and composition. The behavior of the peak with U/V_{RMS} is graphically illustrated by Fig. 10 in which the central spectrogram is a composite of the top and bottom. Finally, it will be noted that the curvature at base and summit at the left side of the peaks is more pronounced than the right side, which again follows from the more gradual recession of the mass line from the stability limit at the low mass end as seen in Fig. 4.

From Eq. (4.2.9), the maximum attainable resolution for nitrogen with an injection potential of 45 volts would be expected to be approximately 24. Test results, however, yield a resolution of about 18 for nitrogen at 95% transmission. This smaller value is probably due to the incompatibility of Eqs. (4.2.2) and (4.2.3) already discussed in Section 4.2. The current obtained with this model, normalized to a pressure of 1×10^{-5} mm Hg was 0.5×10^{-10} amperes at a 40-volt electron beam of about 2.3 ma. (It should be noted that no attempt toward an efficient ion source was made in this model.)

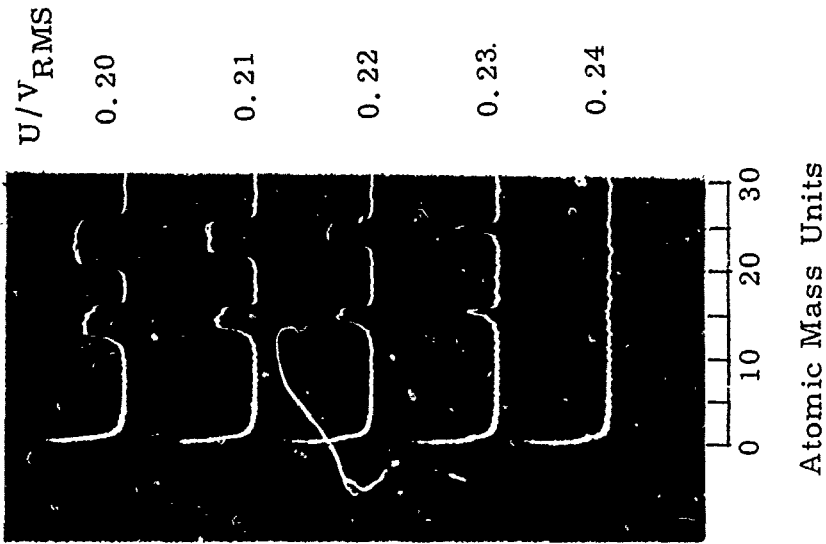


Fig. 9. Massenfilter spectrograms: resolution as a function of U/V_{RMS} . $R_0 = 0.206$ in.; freq. = 2.39 Mc; $D_{in} = 0.031$ in.; $\theta = 5.2^\circ$; $V_{in} = 45$; $P = 4.7 \times 10^{-5}$ mm Hg. (Total Indicated)

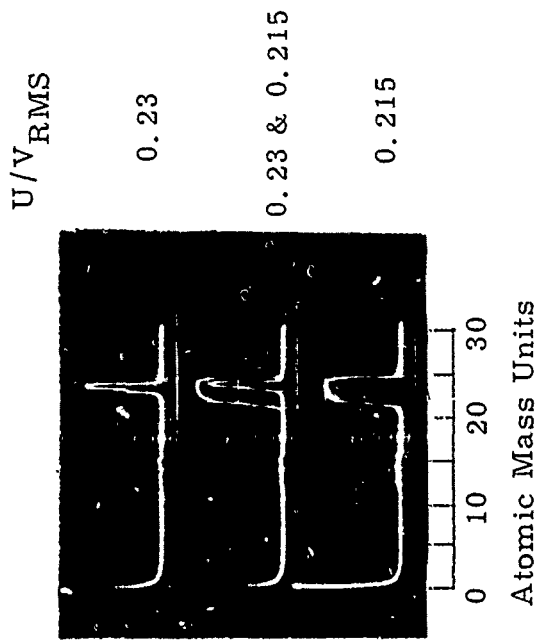


Fig. 10. Massenfilter composite N_2 spectrograms: resolution and peak shape as functions of U/V_{RMS} . $R_0 = 0.206$ in.; freq. = 2.39 Mc; $D_{in} = 0.031$ in.; $\theta = 5.2^\circ$; $V_{in} = 35$; $P = 4.4 \times 10^{-5}$ mm Hg.

An investigation of the effect of injection voltage, V_{in} , on resolution resulted in the spectrograms of Fig. 11 which were taken at a ratio U/V_{RMS} of 0.23. Since the electron beam voltage was the same as the ion injection voltage throughout (both being derived from the same source of potential), the ion currents varied considerably throughout this series of spectrograms and the circuit sensitivity was adjusted in each case to give peaks of the same height. From Fig. 10, we infer that the transmission of Fig. 11 was approximately 95%. It will be noted that, as the injection voltage was reduced the peak narrowed somewhat. A more pronounced effect is the sharpening of the base intercepts of the peak which is of importance in separating and identifying adjacent masses of widely different abundances. A clearer indication of the differences in peak shape is given by the composite spectrogram of Fig. 12, a repeat of selected spectrograms of Fig. 11. In both figures, the small peak at mass number 17 is the residual unidentified gas in the system. Numerical data obtained from Fig. 11 are plotted in Fig. 13. Here in graphic form, the large percentage change in resolution as defined at 5% peak amplitude is clearly evident as compared with the change at half-amplitude.

At this point, it may be well to note from Eq. (4.2.9) that a reduction of V_{in} is equivalent to lengthening the rods. If one wishes to maintain V_{in} at 45 volts and have the base resolution achieved at, say, 22-1/2 volts, he can accomplish this by increasing rod length by $\sqrt{2}$ or by 41%.

In addition to the ability to resolve masses, the correct reproduction of mass abundance is an important property to investigate. Figure 14 shows the spectrogram obtained with Ne^{20} and Ne^{22} . Theoretically, Ne^{22} exists in the amount of 10.8% of Ne^{20} . In the center spectrogram, the gain of the system was increased by a factor of 5 to facilitate in determination of the height of the Ne^{22} peak. The bottom spectrogram is a repeat of the top to verify absence of drift in pressure or circuit gain. Again, from Fig. 10 and the U/V_{RMS} ratio of 0.23 which was used, we infer that transmission in the spectrograms of Fig. 14 was 95% (or better since neon is lighter than nitrogen and has a higher velocity). Within the limits of observational accuracy, Fig. 14 indicates that Ne^{22} is 10% of Ne^{20} . The difference between the observed and handbook ratio may be due to nonlinearities in the scope presentation, a departure of the gain increase from a factor of 5 or a variation in the percent transmission of the two masses. (If any departure from 100% exists, the heavier gases will depart further than the lighter.) Only about 10% of the difference might be attributable to the composition of the neon sample itself.

4.4.2. Variation of Design Parameters.—The effect of inlet port conditions on resolution and current were next investigated. As inlet conditions are extended, i.e., wider angles and larger ports used, a larger ion current will be achieved at the expense of resolution at 100% transmission. Accordingly, a compromise between high current and high resolution must be made. This series of tests was undertaken to aid in making such a compromise.

The various inlet port configurations tested are summarized in Table III.

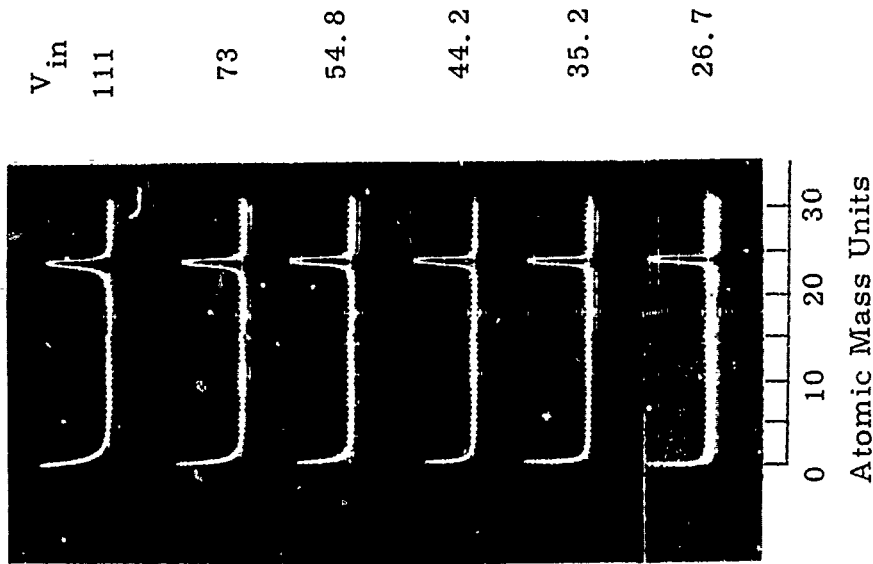


Fig. 11. Massfilter N_2 spectrograms: resolution and peak shape as functions of V_{in} . $R_0 = 0.206$; freq. = 2.39 Mc; $D_{in} = 0.031$ in.; $\theta = 5.2^\circ$; $U/V_{RMS} = 0.23$; $P = 4 \times 10^{-5}$ mm Hg.

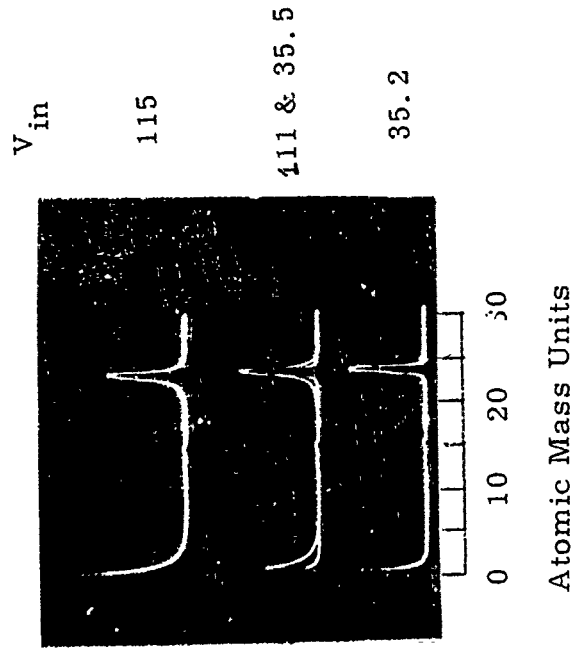


Fig. 12. Massfilter composite N_2 spectrograms: resolution and peak shape as functions of V_{in} . $R_0 = 0.206$ in.; freq. = 2.39 Mc; $D_{in} = 0.031$ in.; $\theta = 5.2^\circ$; $U/V_{RMS} = 0.23$; $P = 4.4 \times 10^{-5}$ mm Hg.

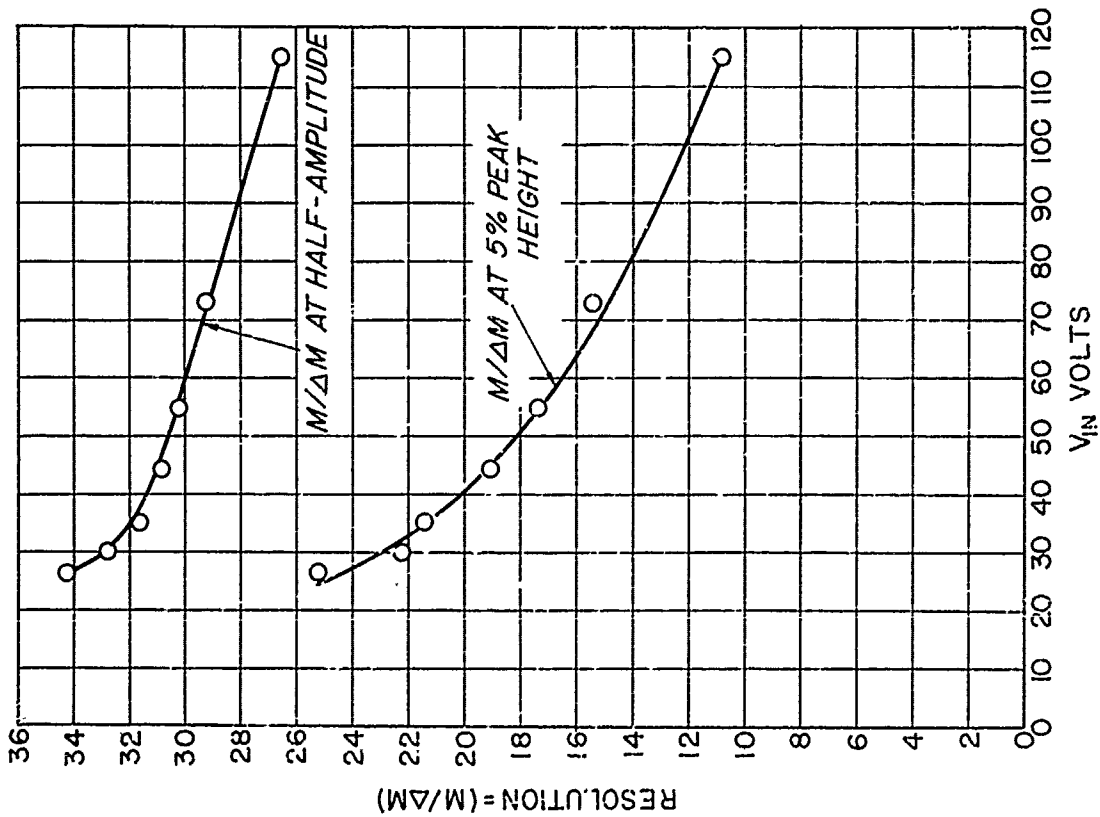


Fig. 13. Massenfilter resolutions as functions of V_{in} . $D_{in} = 0.031$ in.; $\theta = 5.2^\circ$; $U/V_{RMS} = 0.23$; $P = 4 \times 10^{-5}$ mm Hg; gas = Ne_2 .

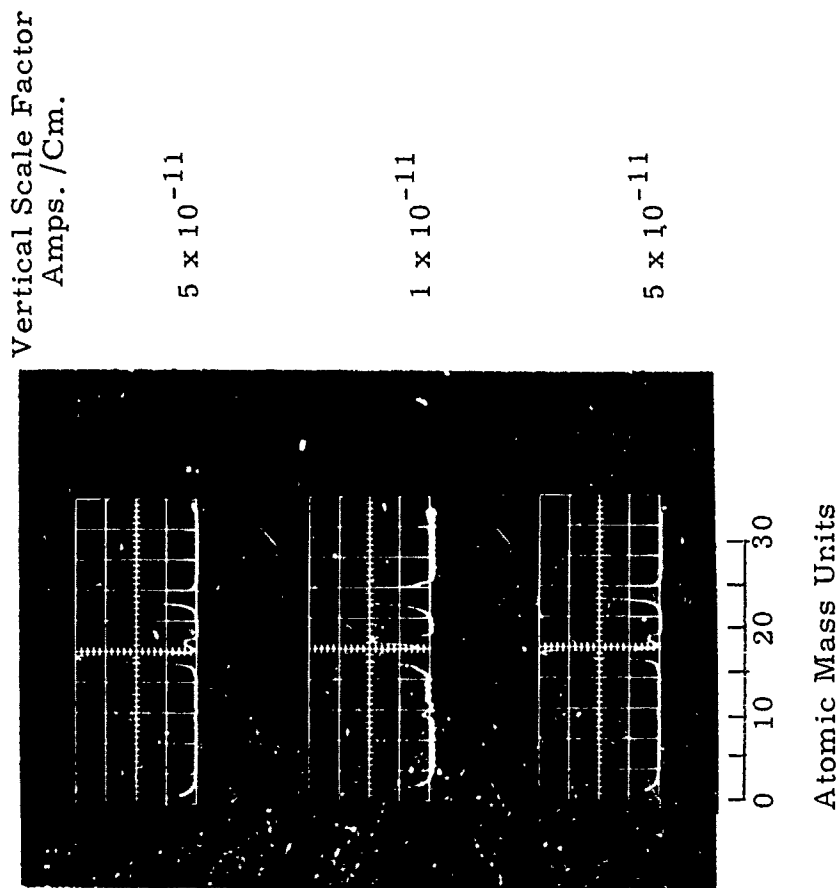


Fig. 14. Massenfilter spectrograms: abundances of Ne^{20} and Ne^{22} . $R_0 = 0.206$ in.; freq. = 2.39 Mc; $D_{in} = 0.031$ in.; $\theta = 5.2^\circ$; $U/V_{RMS} = 0.23$; $V_{in} = 42$; $P = 3.2 \times 10^{-4}$ mm Hg. (Total Indicated)

TABLE III

INLET PORT CONFIGURATIONS

<u>D_{in}</u> (Inches)	<u>θ</u> (Degrees)
0.031	5.2
0.031	6.5
0.0145	5.0
0.0145	2.2
0.062	5.0
0.062	7.8

Reducing D_{in} to 0.0145 in. while maintaining θ at 5° resulted in no appreciable increase in resolution. Ion currents dropped to slightly less than 25% of their former value or about in the same ratio as the reduction in inlet area. Next, a reduction in inlet angle, θ , 2.2° resulted in a slight improvement in resolution from 18 to 20 but made no significant change in ion currents. The inference to be drawn is that the ion stream impinging on the center of the inlet port is essentially axial in direction although no further evidence exists to verify this statement.

Since no great gain in resolution resulted from restrictions of inlet conditions below design values, perhaps a relaxation of inlet conditions will yield a larger ion current without a great sacrifice in resolution. Accordingly, the original port was widened to an angle of 6.5° maintaining the exit diameter at 0.031 in. The half-amplitude resolution for nitrogen dropped from 18 to 12 while the current increased from 0.5×10^{-10} amperes to 0.8×10^{-10} amperes. This configuration, then, shows no promise of any advantage. It was used, however, to gather the data presented in Fig. 15 which illustrates the dependence of ion current and resolution on the ratio U/V_{RMS} and also shows the method by which resolution at 95% transmission was determined.

As a final step, the injection port diameter was opened to 0.062 in. and tested at values of θ equal to 5° and 7.8° . While a large decline in resolution from 18 to 13 was noted at 5° , no increase in ion current was observed. Caution must be used in this observation, however, since the inlet port configuration had to be changed to limit the angle to 5° . At $\theta = 7.8^\circ$, a further decrease in resolution to 8 was observed while the peak current increased to 2.8×10^{-10} amperes. While the increase in ion current is desirable, a resolution of 8 is considered unacceptable.

All these results are shown in graphic form in Figs. 16 and 17. Results are too few to justify the presentation of a curve; however, related points are connected by a dotted line. It does appear, however, that the original inlet port design parameters result in the best overall operation.

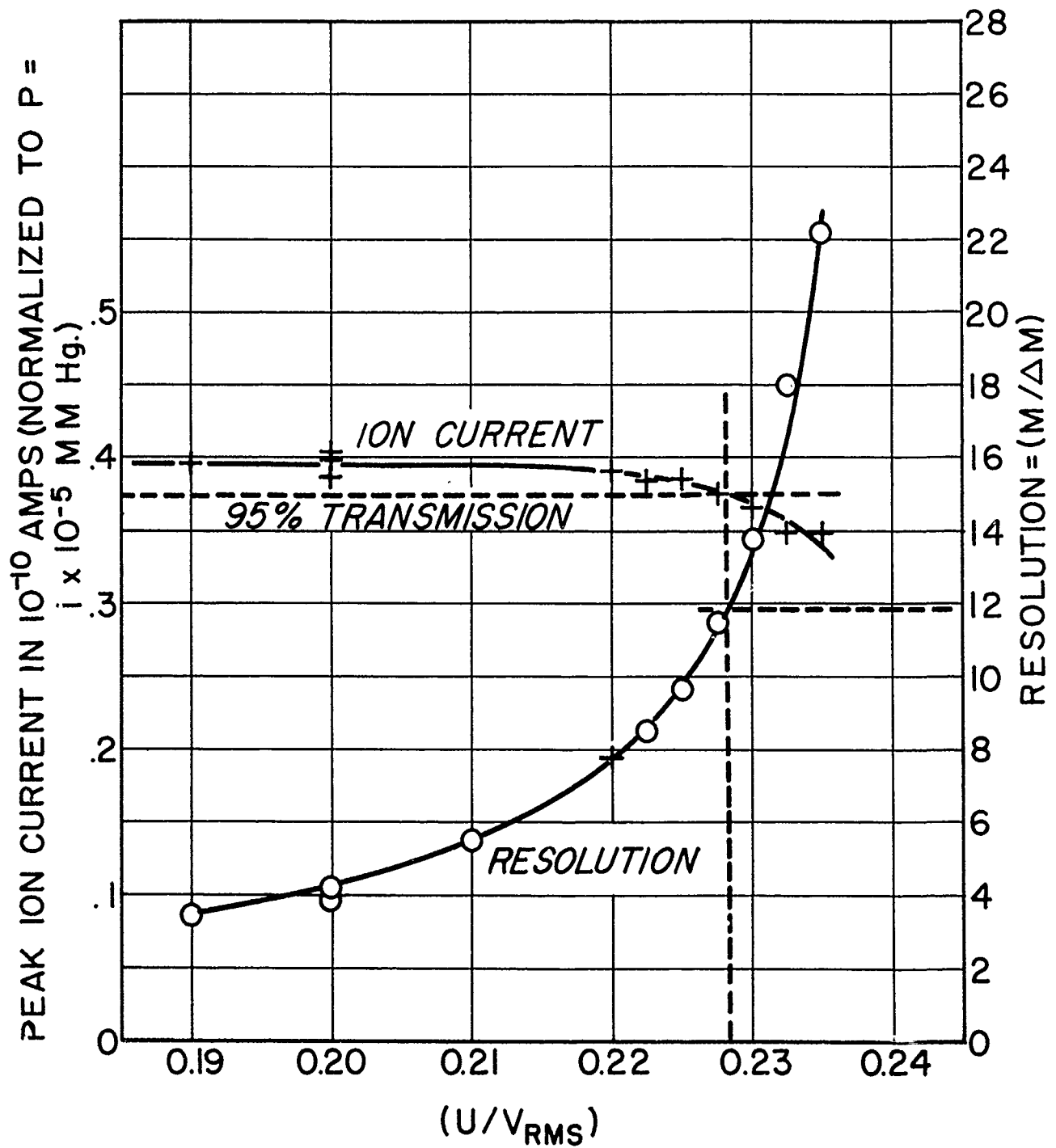


Fig. 15. Massenfilter resolution and peak ion current as functions of U/V_{RMS} . $D_{in} = 0.031$ in.; $\theta = 6.5^\circ$; $V_{in} = 40$ volts; $P = 6 \times 10^{-5}$ mm Hg; gas = N_2 .

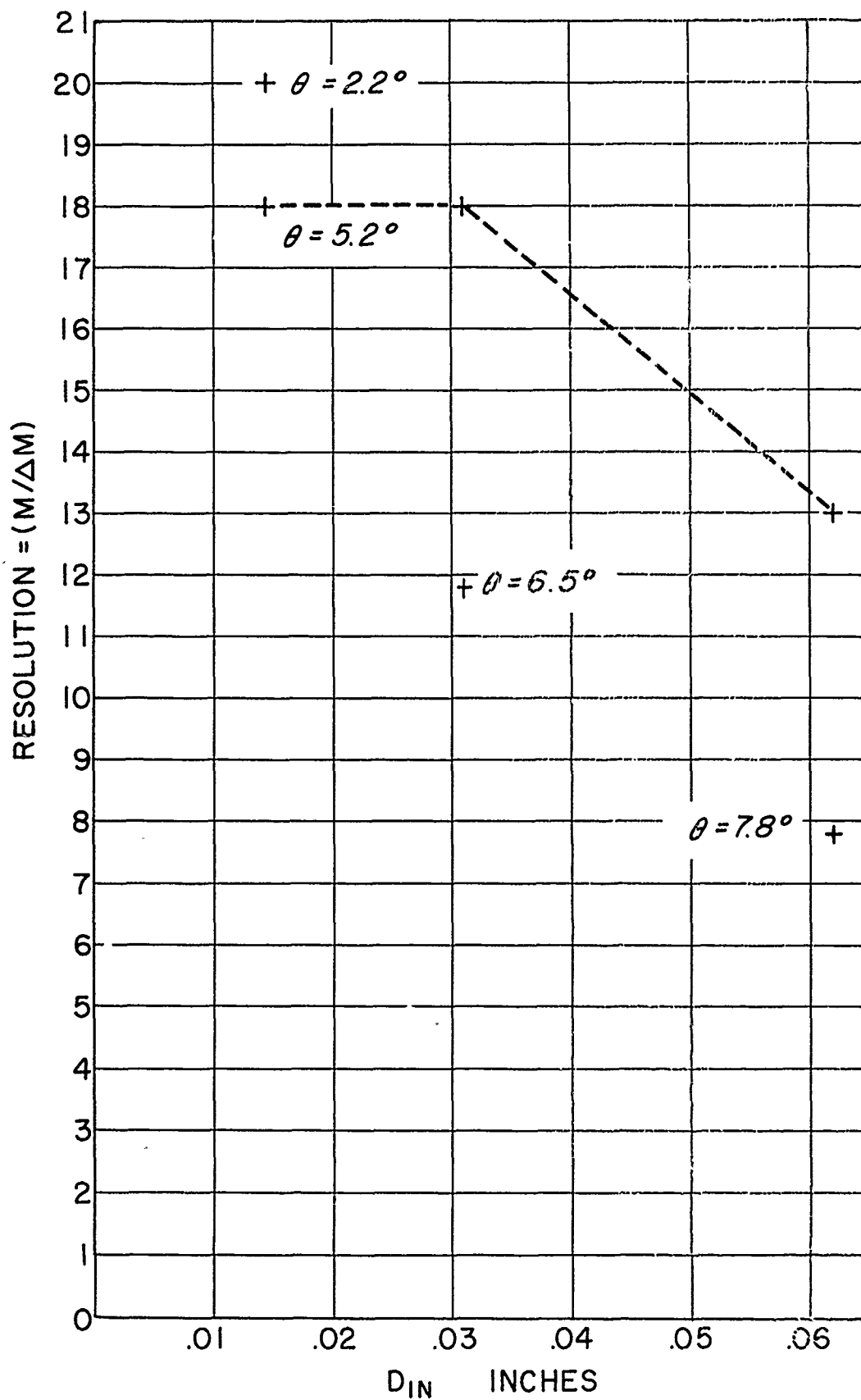


Fig. 16. Massenfilter resolution as a function of inlet port configuration. $V_{in} = 40$ volts; gas = N_2 .

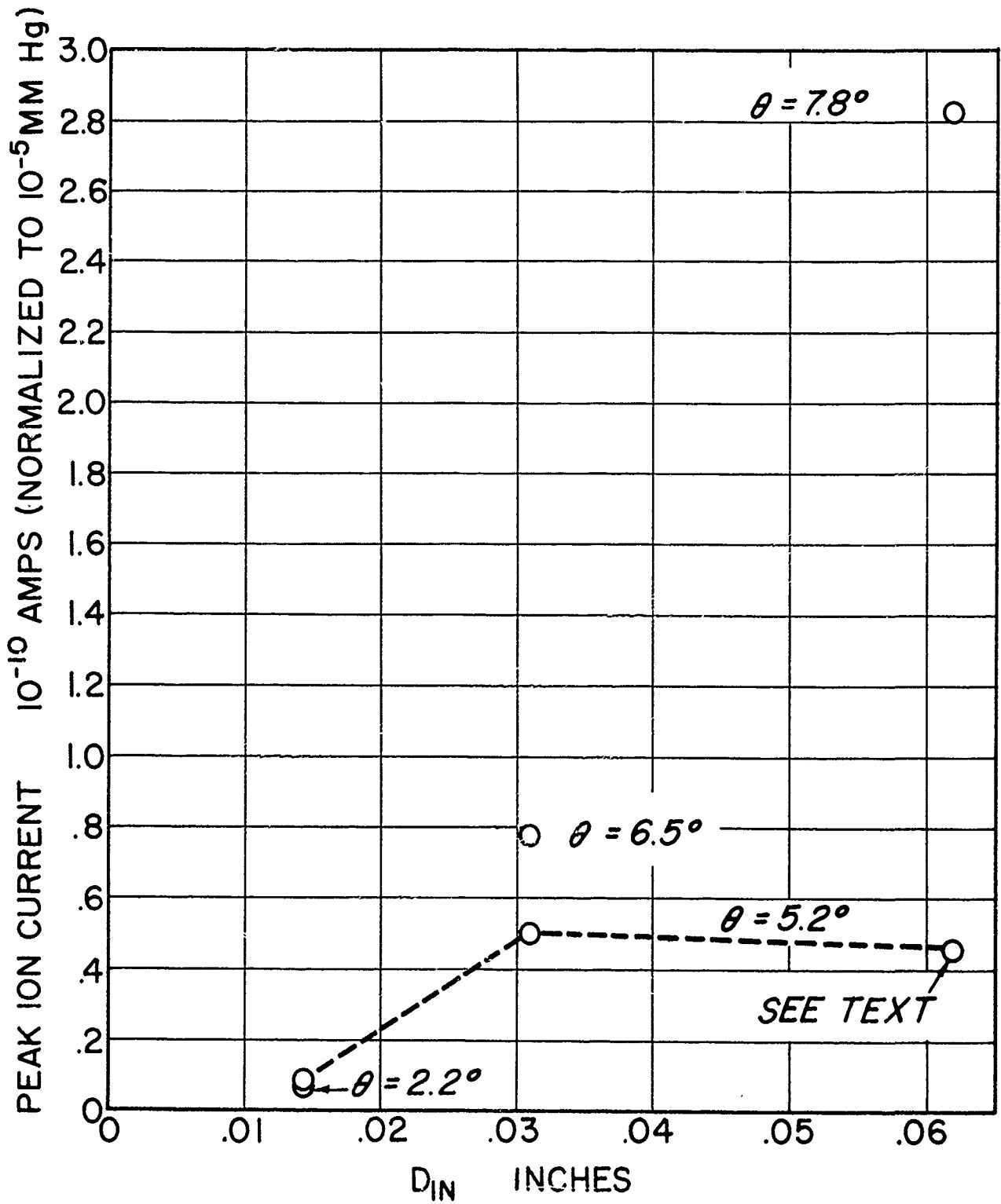


Fig. 17. Massenfilter ion current as a function of inlet port configuration. $V_{in} = 40$ volts; gas = N_2 .

In summary, then, it appears that the initial design is perfectly adaptable to flight. Essentially the same values of θ and D_{in} will be used in the flight model. Aside from changes in the ionizing section to be described and changes in mechanical detail, the only change anticipated in the flight design may be a 50% increase in rod length to obtain better resolution at the base of the peak as discussed earlier.

4.5. FLIGHT MODEL DESIGN

Translation of laboratory results to a flight model design has been initiated. The massfilter may be divided into roughly four sections—the collector, the analyzing section, the ionization volume, and the electron source. At present, a further investigation of the latter two appears to offer the best promise of increased sensitivity—highest ratio of ion current to ambient density.

4.5.1. Ionization Volume.—Two major improvements in the design of the ionization volume appear possible at this writing. In the present laboratory design, a large fraction of the available electrons are probably impinging directly on the "hat" rather than falling through the orifices into the volume where useful ionization can occur. In addition, no attempt has been made to focus these electrons to the axis of the instrument where the created ion has the greatest probability of arriving at the inlet port within the necessary restricted inlet conditions. The second major possible improvement lies in designing the ionization source to focus more effectively those ions that are formed on the inlet orifice.

The flight model will replace the "hat" and orifice arrangement used in the laboratory design with a volume enclosed by a fine grid. Two distinct advantages should result: more efficient utilization of the electrons emitted by the filament since a greater fraction will enter the ionizing volume, and a major reduction in the probability of a neutral molecule experiencing a collision with the apparatus prior to being ionized. This latter point will be discussed in more detail in a later section. In addition, cylindrical symmetry will focus the electrons on the axis where ionization is most efficient from a sensitivity standpoint.

Direction of the created ions to the inlet port is to be accomplished by the use of the cylindrical lens system common to cathode-ray-tube electron guns. In this manner, a greater percentage of the created ions will reach the inlet port within the limited inlet conditions demanded by the analyzing section.

Preliminary work along these lines has been initiated. Figure 18 is a view of the components of the cylindrical lens system currently under test. The electron accelerating grid can be seen on the near end of the cylinder located second from the left. Assembled, this grid is coaxial with a circular filament around the outside. The two cylinders to the right are sections of the lens system and the small disks comprise a slotted collector so designed to facilitate in determining beam cross section. The large cylinder on the left serves as a filament



Fig. 18. Laboratory cylindrical lens components.

shield and has been incorporated for experimental reasons. Its need in the flight model is considered unlikely. The slots which are apparent in the larger cylinders are only for the purpose of restricting heat flow from the filament to the Teflon mounting plate.

The unit has been assembled and is currently under test. Results will be reported at a future date. For reasons to be discussed, the final design will replace the solid cylinders with grid structures.

4.5.2. Electron Source.—A large increase in ion current as a function of ambient pressure can obviously be realized by increasing the electron emission. The laboratory massenfilter has been operated at about 2.5-ma emission and a factor of ten should be easily realizable. Two of the important properties of the filament are the necessary heating power and the behavior in an environment containing oxygen.

Under the dynamic conditions of flight, loss of oxygen by chemical combination with the filament is not considered detrimental in itself. Indeed, any nascent oxygen which impinges on a surface prior to ionization will give rise to an erroneous composition determination due to recombination. In a laboratory system for calibration and test purposes, however, a filament which reacts at the slowest possible rate with oxygen is highly desirable. In either case, continuous operation of the filament under ambient conditions is mandatory.

In the work heretofore reported, tungsten filaments were used as the source of electrons. At operating temperatures, the WO_3 formed by chemical reaction evaporates off the filament. Hence any gas is quickly depleted of its oxygen content, so that, at the pressure used, only temporary effects on the emission characteristics have been noted. Presently, experiments are underway to investigate the comparative power requirements and oxidation properties of tungsten and thoria-coated iridium filaments. Initial results indicate the iridium filaments lose emission capabilities to a greater extent but recover in a shorter time than tungsten. It is felt that emission regulation by filament temperature will substantially compensate for the changes in work function, so that the advantages of thoria-coated iridium need not be foregone. These advantages are much lower heating power per milliampere emission current and continuous operation at relatively high oxygen partial pressures without failure. Tests are continuing and will be reported in greater detail in a subsequent report.

4.6. ADVANTAGES

A rocket-borne instrument should be light in weight. Obviously, too, it should be reliable. In general, this implies that it should be simple to build and operate. If the instrument is to be used synoptically, these characteristics become mandatory.

Within this frame of reference, analysis of the theory and results of the laboratory experiments indicate the following advantages possessed by the massenfilter:

- (1) Light in wieght since it requires no magnetic field.
- (2) Simple, rugged construction.
- (3) Reliable and repeatable operation without requiring constant and meticalous attention to detail.
- (4) Sensitivity expected to be comparable to the best so far obtained in nonmagnetic mass spectrometers, assuming an efficient ion source.
- (5) Simple supporting circuitry.
- (6) Relatively insensitive to small perturbations.
- (7) Resolution increases with mass number where it is most needed.

In addition, the massenfilter has the ability to work to comparatively high densities which is very desirable in this particular application.

5. OMEGATRON

5.1. PRINCIPLE OF OPERATION

Although a brief elementary description of the omegatron appeared in 1949⁹ and a discussion of the use of resonance absorption techniques to detect resonant ions in the omegatron appeared in 1950,¹⁰ the first comprehensive article with an analysis of omegatron operation appeared in 1951.¹¹ Subsequent articles¹²⁻¹⁵ deal with trajectory analysis and applications of the omegatron. The pertinent theory, taken from the above references, is presented in an appendix for the convenience of the reader.

5.2. DESIGN AND PRELIMINARY TEST

Using the Bennett mass spectrometer, Meadows and Townsend¹⁶ report an analysis of neutral gases above WSPG ranging between mass numbers 14 and 44. This, then, was selected as the minimum range over which any analysis should be considered. Nowhere in this range are any two gases any closer than 2 AMU with the exception of CO₂ and N₂O. Thus a resolution of 20 should be adequate for analyzing the constituents of the upper atmosphere. The omegatron may reasonably be expected to operate to densities where the mean free path and orbital path lengths are of the same order of magnitude. Using the mean free path of 10 cm from Table I at 100 km (the lowest altitude specified in the work statement) and a resolution of 20, Eq. (A17) yields a value of 2.5 mm for R₀. Based on this value and an assumed flux density of 3000 gauss, the working conditions are summarized in Table IV.

TABLE IV

OMEGATRON WORKING PARAMETERS*

Mass No. (AMU)	L (cm)	$\frac{M}{\Delta M}$	n (revs)	E ₀ (mv/cm)	f (kc)	t (μsec)	W (ev)
46	10	20	12.7	117	100	128	0.59
14	10	20	12.7	385	328	39	1.93
1	10	20	12.7	5390	4600	2.8	27

*R₀ = 0.25 cm; B = 3000 gauss.

To approximate the uniform electric fields assumed in their theoretical development, Hipple, Sommer, and Thomas¹¹ formed the cubic analyzing volume of their omegatron with a series of guard rings at each end of which were located the rf plates. The rf voltage was equally divided across the guard rings. Unless accurate correlation with the theory is required, however, simple workable omegatrons have been constructed by other workers¹³⁻¹⁵ by using a simple cubic structure, eliminating the guard rings and accepting the nonuniform electric field gradients. Such was the construction selected; it is illustrated in Fig. 19. Here, electrons are obtained by thermionic emission from the tungsten filament. Those which are emitted at the axis of the instrument proceed down the magnetic field through the holes in the box and finally impinge on the anode. Adjustment of the beam control plate voltage regulates the beam current. Ions created on the axis by the electron beam are acted upon by the rf field created by the plates and those which are in resonance reach the collector and are measured by the electrometer. To repel the ions from the ends of the box, a small positive "trapping" voltage, typically a few tenths of a volt, is applied to the box.

The original unit built in our laboratory had all elements supported on their leads. This proved unsuccessful due to the difficulty of maintaining proper alignment and led to the unitized construction shown in Figs. 20 and 21. Not shown in these figures is the collector which was supported by the glass tubulation and projected in from the side. The rf plates and end faces form a box approximately 7 mm³. R_0 was adjusted to 2.5 mm. Results with this model were inconclusive owing to their highly variable nature. Figure 22 illustrates the type of spectra obtainable with this unit. The mass scale of Fig. 22 is derived from Eq. (A3) using the measured value of 2750 gauss for flux density. The gas was nitrogen and the lack of resolution and the erroneous location of the peak is self evident. Inadequate shielding of the ion volume from surface charges accumulating on the glass walls was suspected as a major reason for these difficulties. This led to the construction of the enclosed model shown in Fig. 23. The collector protruded through the slot visible in this figure. In this manner tests of a rigid model of flight dimensions were initiated.

In support of the program, the Reuter-Stokes Company, Cleveland, Ohio, was contracted to build a fully shielded omegatron (Fig. 24) in which the elements were supported by the leads. Other features differed only in detail from the unit of Fig. 23. Only a small fraction of the total filament emission current was available in the beam, presumably because of misalignment of the holes. Nevertheless, a series of tests was made which yielded results comparable with those obtained from the other omegatrons at that time. The spectrum obtained for helium is shown in Fig. 25 and those for neon, nitrogen, and argon in Fig. 26. The small peak at 12-13 mass units in Fig. 26 is presumed to be due to doubly ionized nitrogen. While the resolution in these latter two figures is still inadequate, it is significantly better than that obtained with the first model. In addition, there is much better agreement between the theoretical mass scale and the position of the peaks. Table V

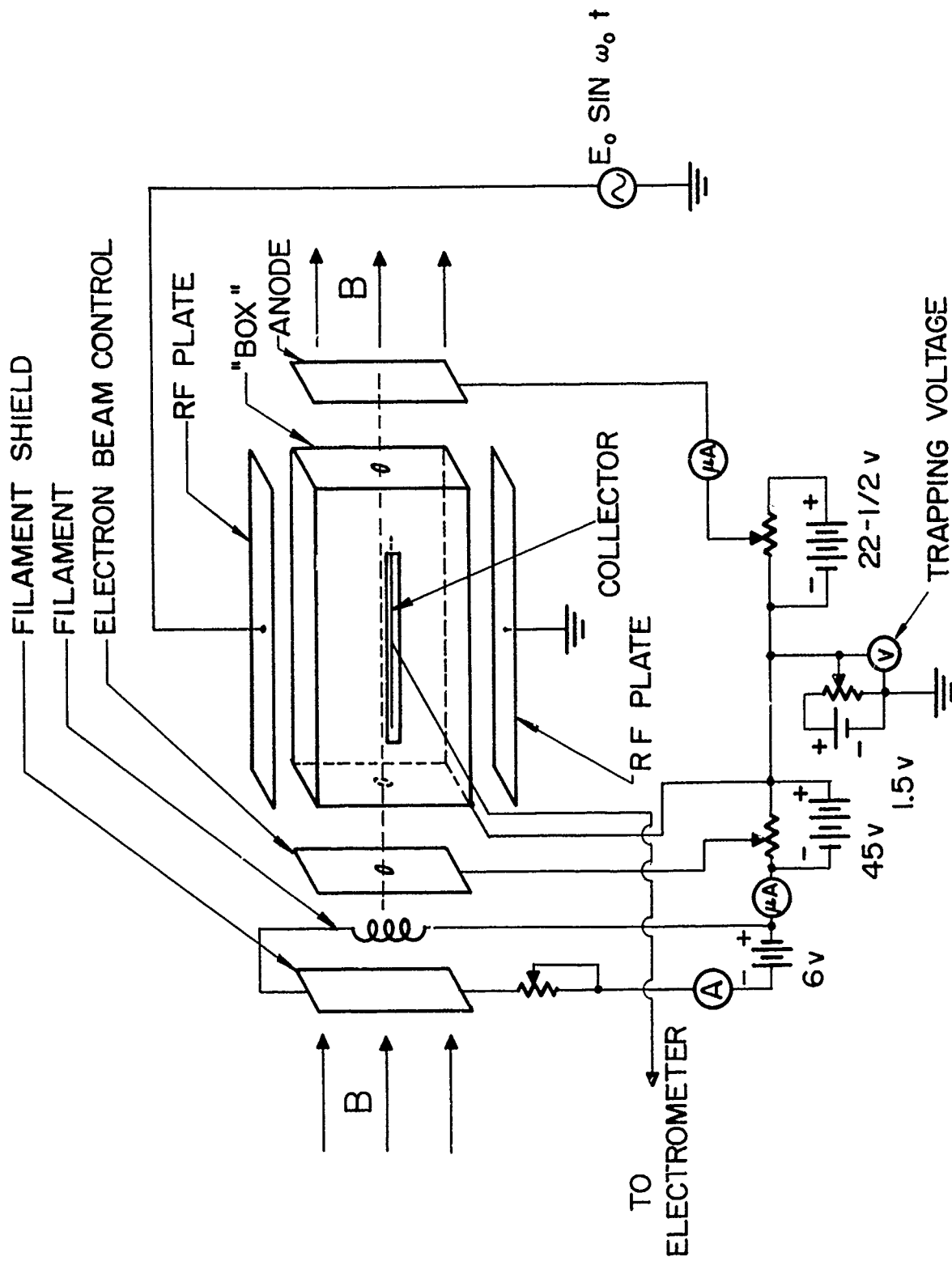


Fig. 19. Omegatron schematic.

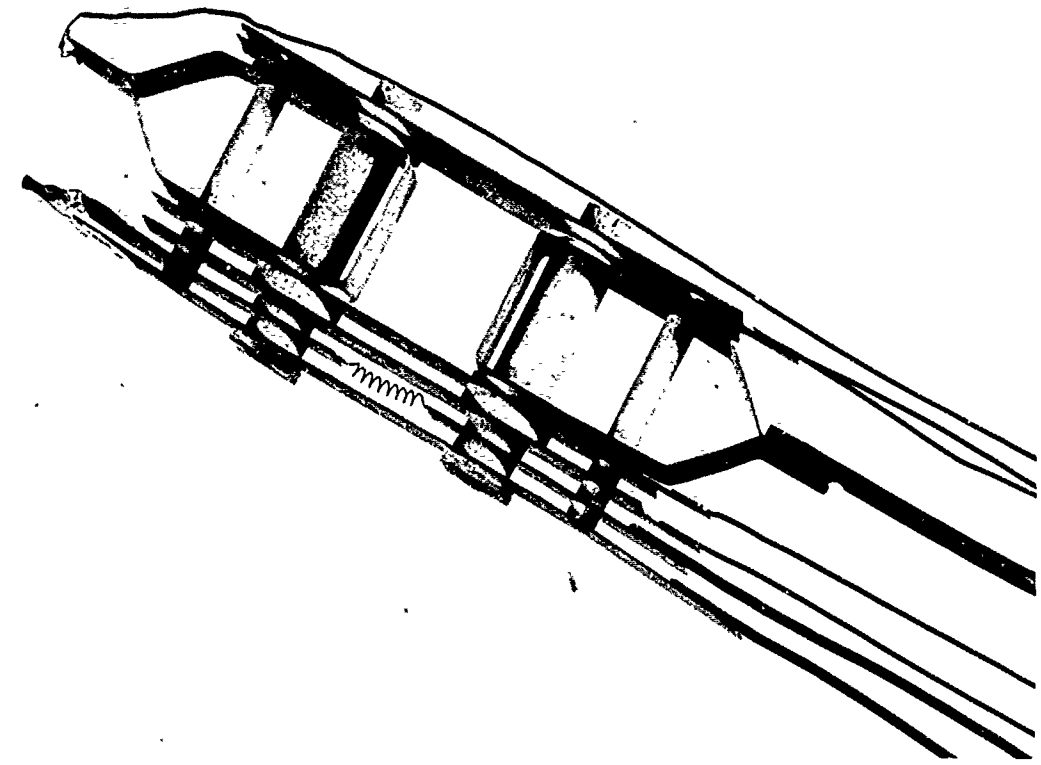


Fig. 21. Open-box omegatron closeup.

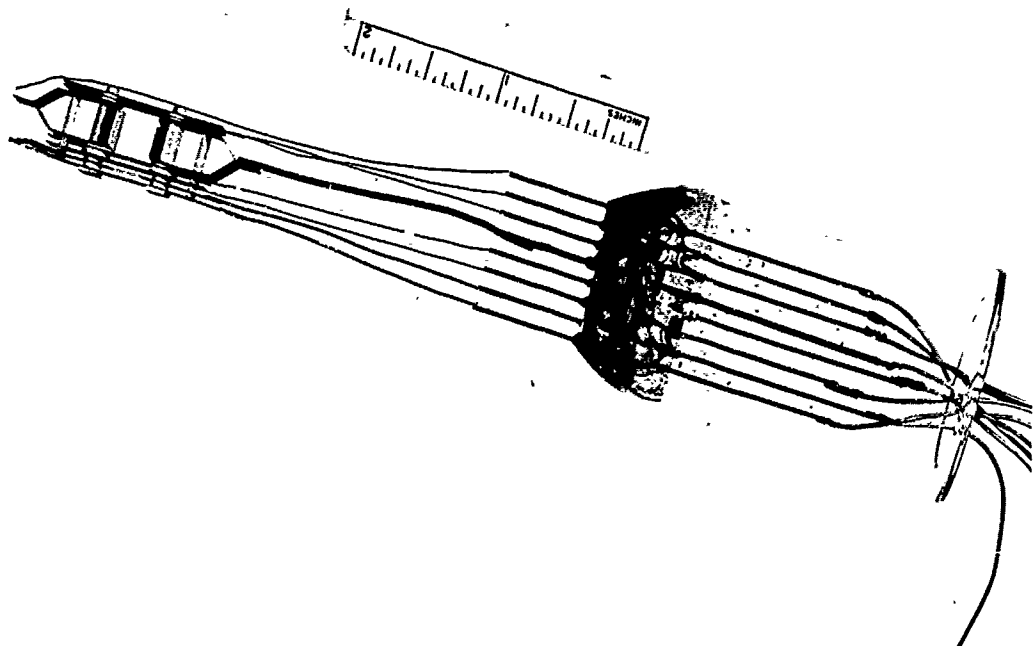


Fig. 20. Open-box omegatron.

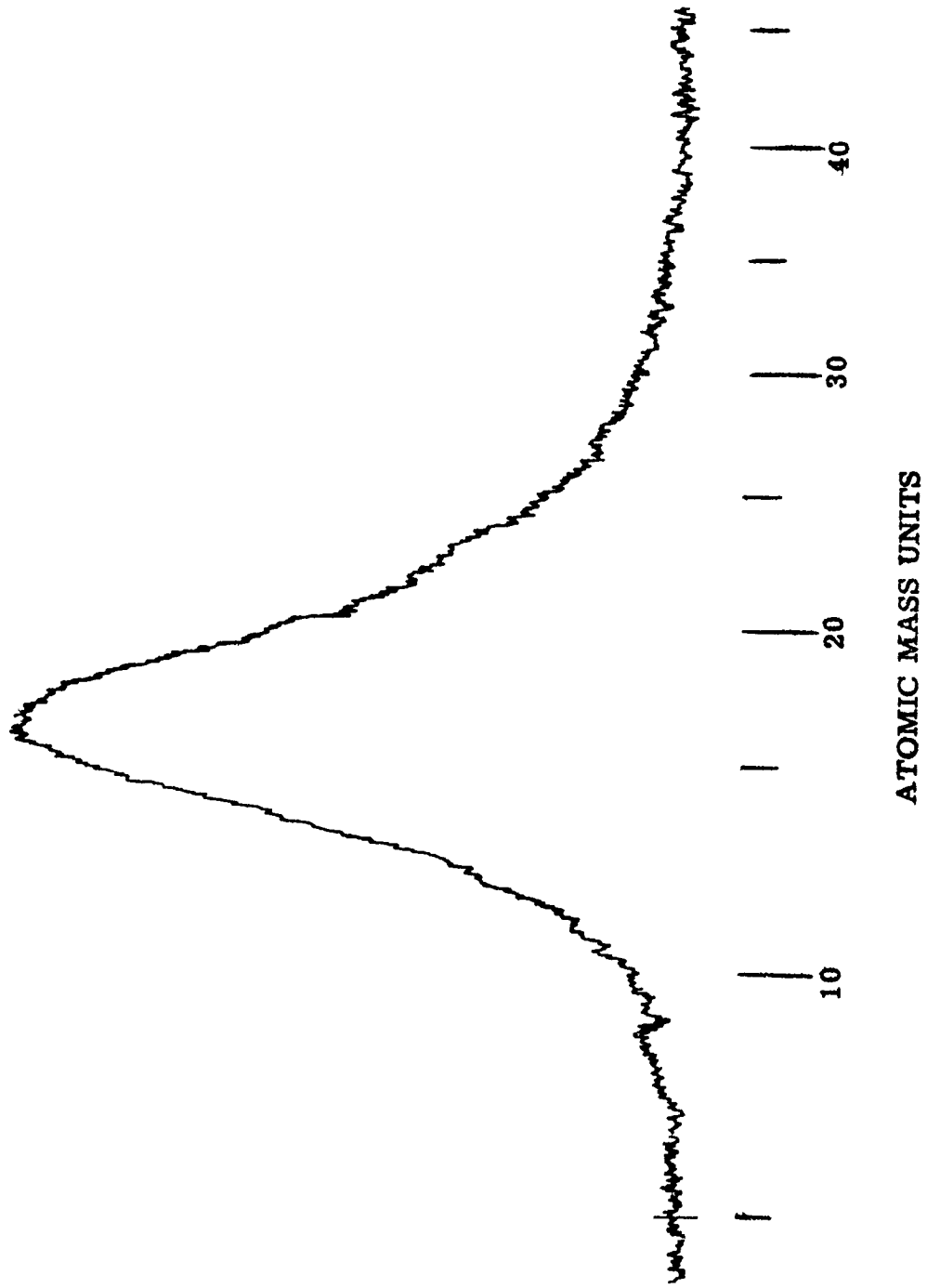


Fig. 22. Open-box omegatron spectrum.

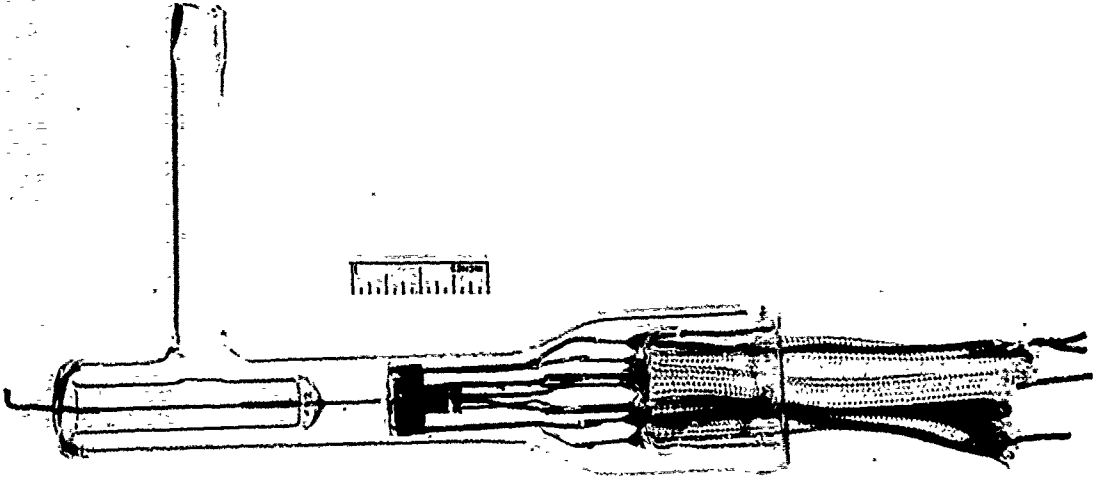


Fig. 24. Commercial omegatron.

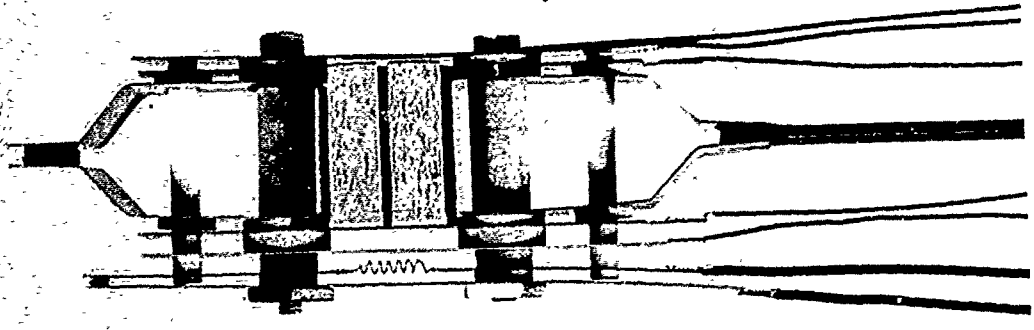


Fig. 23. Enclosed omegatron.

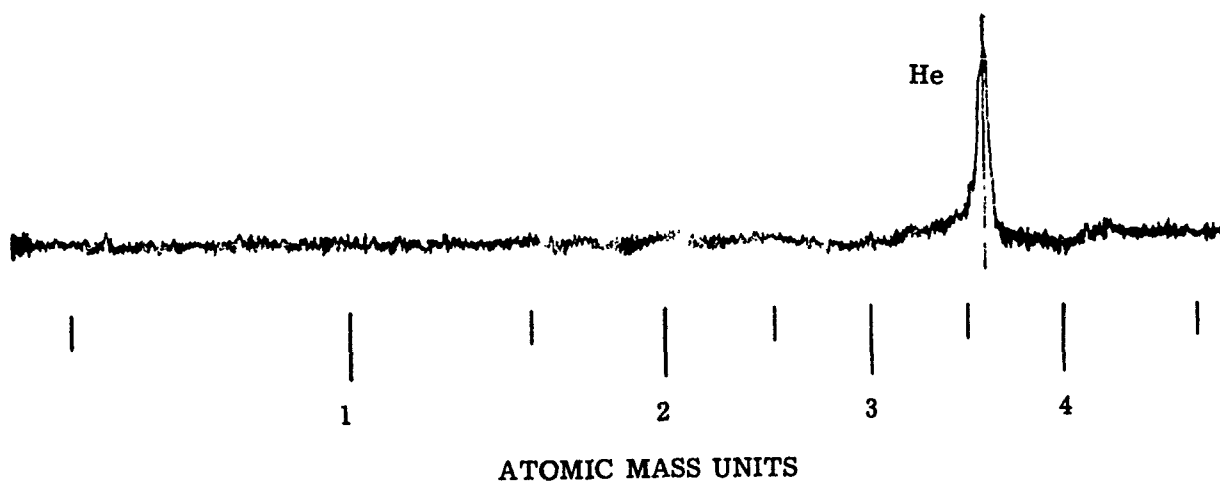


Fig. 25. Helium peak, commercial omegatron.

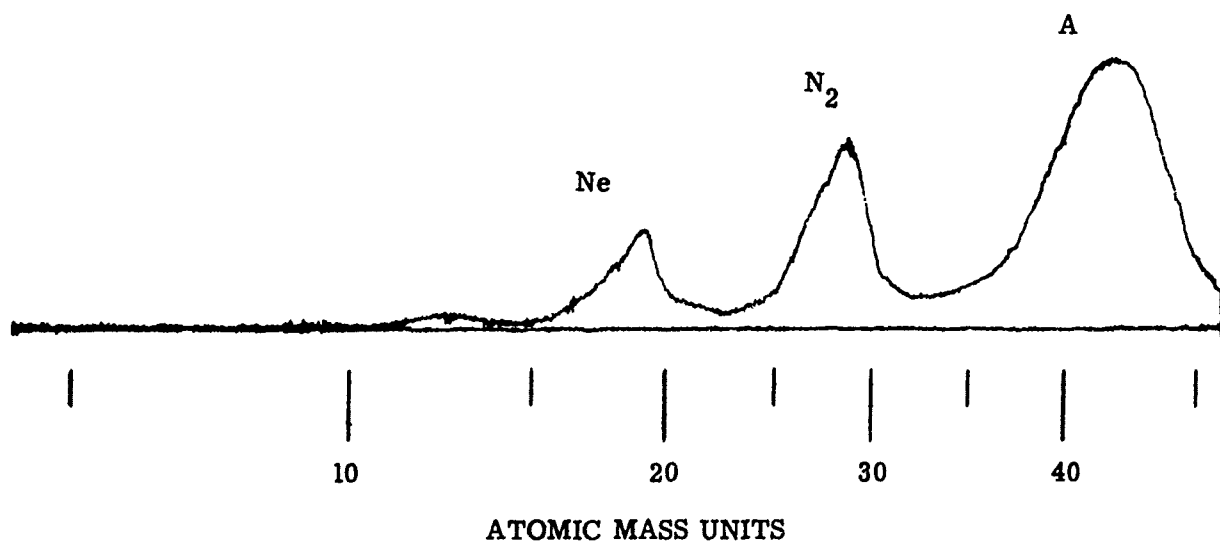


Fig. 26. Ne, N₂, and A spectrum, commercial omegatron.

compares the resolution determined from Eq. (A13) with that estimated from Figs. 25 and 26.

TABLE V
COMPARISON OF EXPERIMENTAL AND PREDICTED RESOLUTIONS

Gas	$\frac{M}{\Delta M}$ [Eq. (A13)]*	$\frac{M}{\Delta M}$ (Figs. 25 and 26)
Helium	19.6	11.6
Neon	3.9	2.2
Nitrogen	2.8	2.6
Argon	2.0	2.9

* $E_0 = 1.16$ volts/cm
 $P_T = 2 \times 10^{-6}$ mm Hg
 $B = 2750$ gauss
 $R_0 = 0.25$ cm

5.3. TESTS OF FINAL MODEL

Most of the tests were run on the model of Fig. 23. In these tests a number of parameters were varied such as magnetic flux density and direction; E_0 and the manner of application (single-ended drive to either plate and balanced drive); electron beam current; trapping, anode and beam control voltages; drift voltage; pressure of the gas sample and R_0 . Following considerable experimentation, it was determined that best results were obtained with an electron beam of 2 to 3 microamperes and 45 volts energy, with a trapping potential of approximately 0.3 volt, with a single-ended rf drive to a plate which depended on the magnetic field direction, with the highest magnetic flux density (4300 gauss in this case) and with anode and electron beam controls at box potential. Theoretically, the potential of these two electrodes should have no effect on the performance of the analyzing section if the electron beam current is adjusted to the prescribed values. In practice, however, the potentials of the beam control electrode and the anode had a significant effect on the spectra obtained presumably because of the radial fields which protruded into the box through the adjacent holes.

Reference (14) shows that the resonant frequency of an ion subjected to an additional radial electric field is given by

$$\omega_r = \frac{eB}{m} - \frac{E_r}{Br} \quad (5.3.1)$$

where

r is the trajectory radius at any instant,
 ω_r is the angular resonance frequency at radius r , and
 E_r is the radial electric field strength at radius r .

Thus, unless E_r/r is a constant or the entire second term is negligible, the instantaneous resonant frequency of an ion is a variable function of its orbital radius. This term, therefore, not only results in an apparent mass shift but sets an upper limit on the attainable resolution. This comes about since, at low E_0 , an ion entering a resonant spiral path at the center becomes nonresonant at larger radii, gets out of phase, returns to a smaller radius, and never reaches the collector. Equation (5.3.1) indicates the relative effects are greater at high mass numbers. For example, a 10% change in ω for argon occurs when E_r/r is only 2 volts cm^2 —a value easily reached in the vicinity of the holes when the adjacent electrodes are operated at potentials significantly removed from box potential. Argon ion current is plotted against the applied rf voltage in Fig. 27 and exhibits a definite cutoff value undoubtedly attributable to the radial field.

The second term of Eq. (5.3.1) has two other contributing sources. The first of these is the space charge which results from the electron beam and cloud of nonresonant ions near the axis. Being the slower particles, the ion cloud is the major effect. The radial field strength is inversely proportional to r , so the second term varies as $1/r^2$. For this reason, in practical operation, the ion cloud is minimized by using an electron beam in the neighborhood of microamperes. Attempts to sweep the volume of charge continually by the drift voltage, discussed in Section C of the Appendix, yielded only negative results.

The second contributing source arises from the trapping voltage. While this potential is intended only to prevent axial loss of ions, it also gives rise to radial field components. The upper value of trapping voltage is undoubtedly limited by this effect so that one finds an optimum in the vicinity of a few tenths of a volt which is just sufficient to overcome thermal energies. Figure 28 illustrates the effect of trapping voltage on ion currents plotted as a function of rf drive voltage. It will be noted that the rf "cut-off" voltage increases with trapping voltage but the slope of curves also increases so that higher peak ion currents are obtained with moderate trapping voltage at properly selected drive voltages.

Figures 29 and 30 illustrate some of the best spectra obtained with the omegatron operated under carefully optimized conditions and a magnetic flux density increased to 4300 gauss. The observed resolution of the helium peak of Fig. 29 is 35 while the value predicted by Eq. (A13) is 46. The predicted resolutions for neon, argon, and their isotopes and those observed from Fig. 30 are given in Table VI.

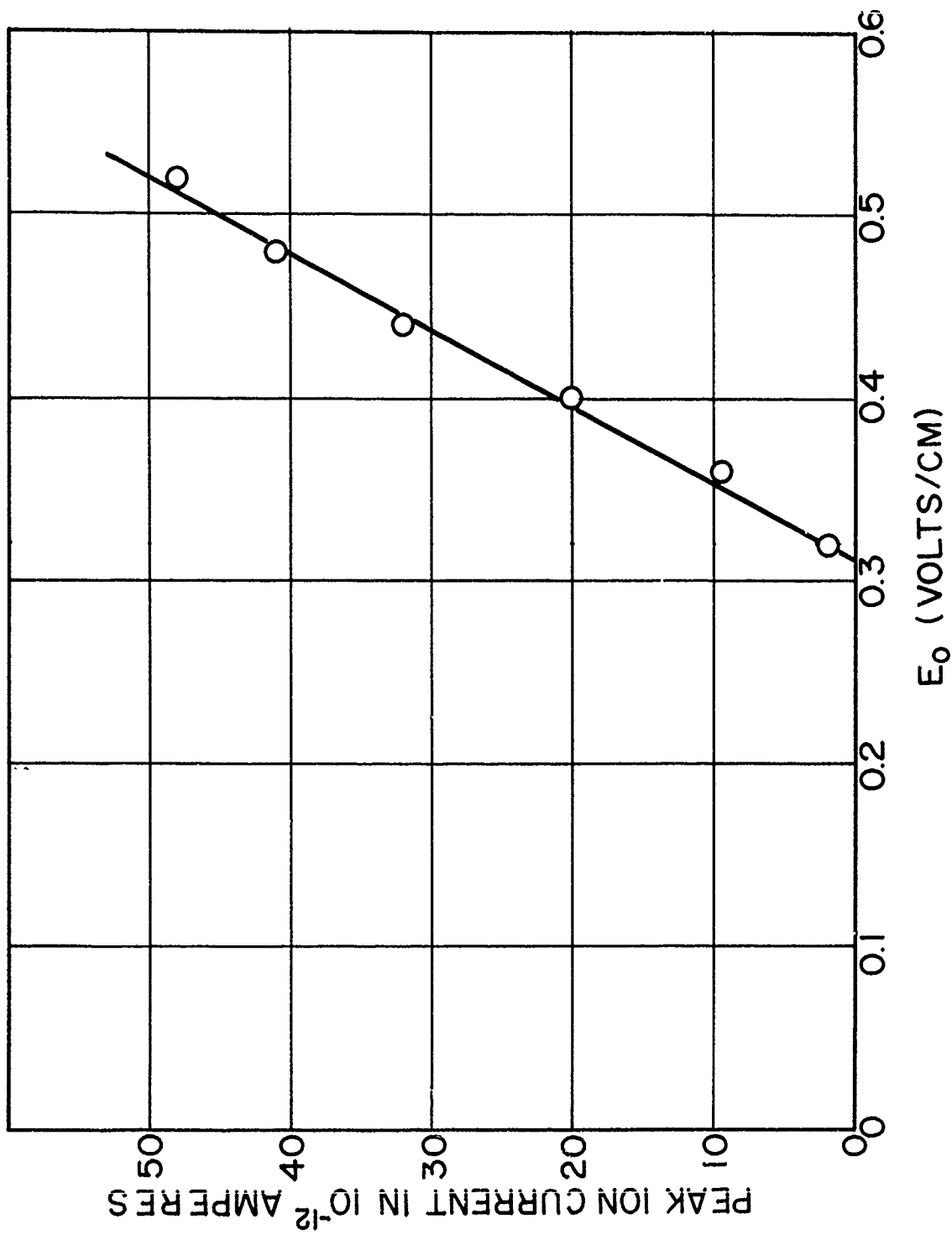


Fig. 27. Peak argon ion current as a function of E_0 . $B = 2750$ gauss; trapping voltage = 0.2; $f = 119$ kc; $R_0 = 0.25$ cm.

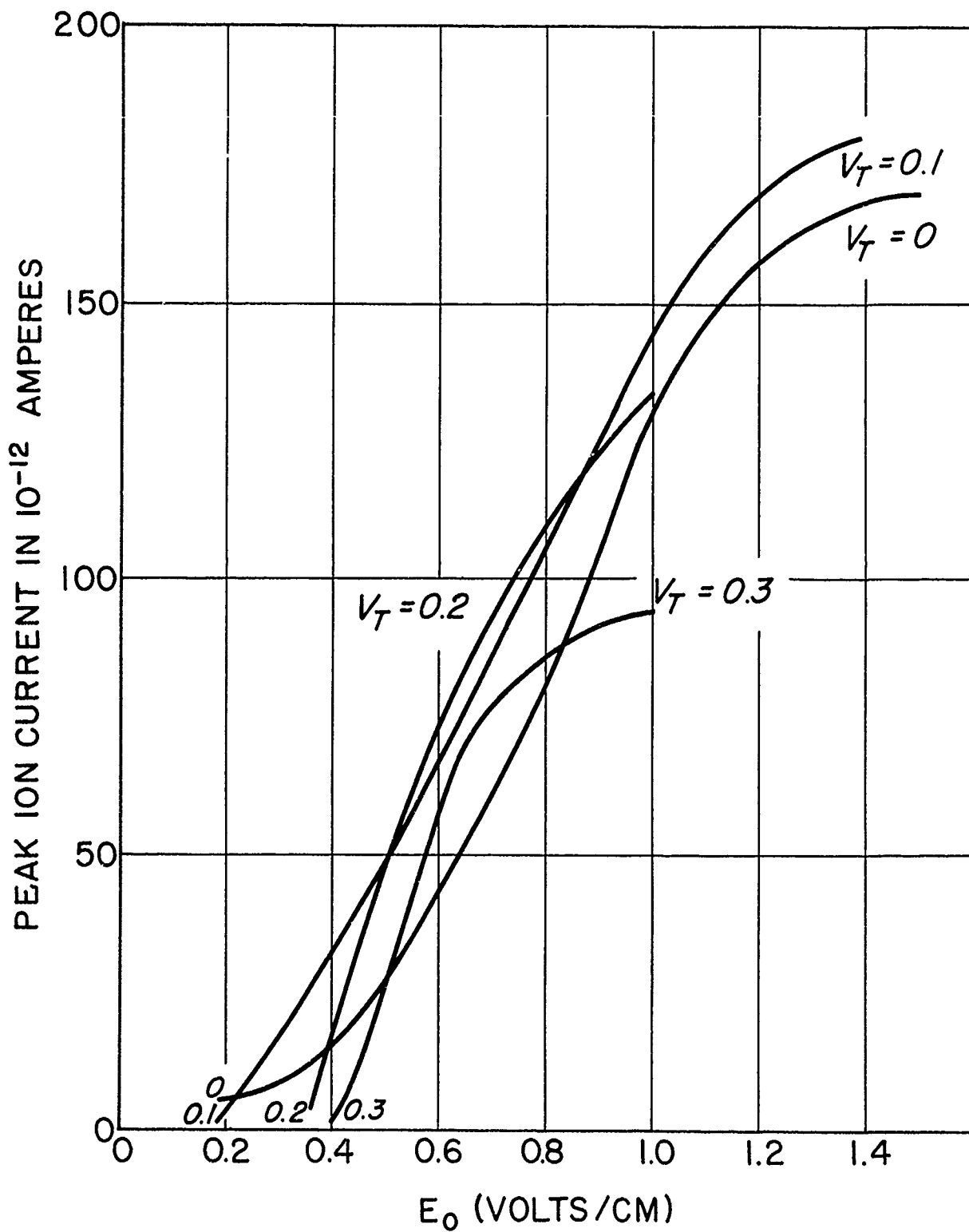


Fig. 28. Peak ion currents as functions of E_0 at various trapping voltages. $B = 2750$ gauss; $f = 119$ kc; $R_0 = 0.25$ cm.

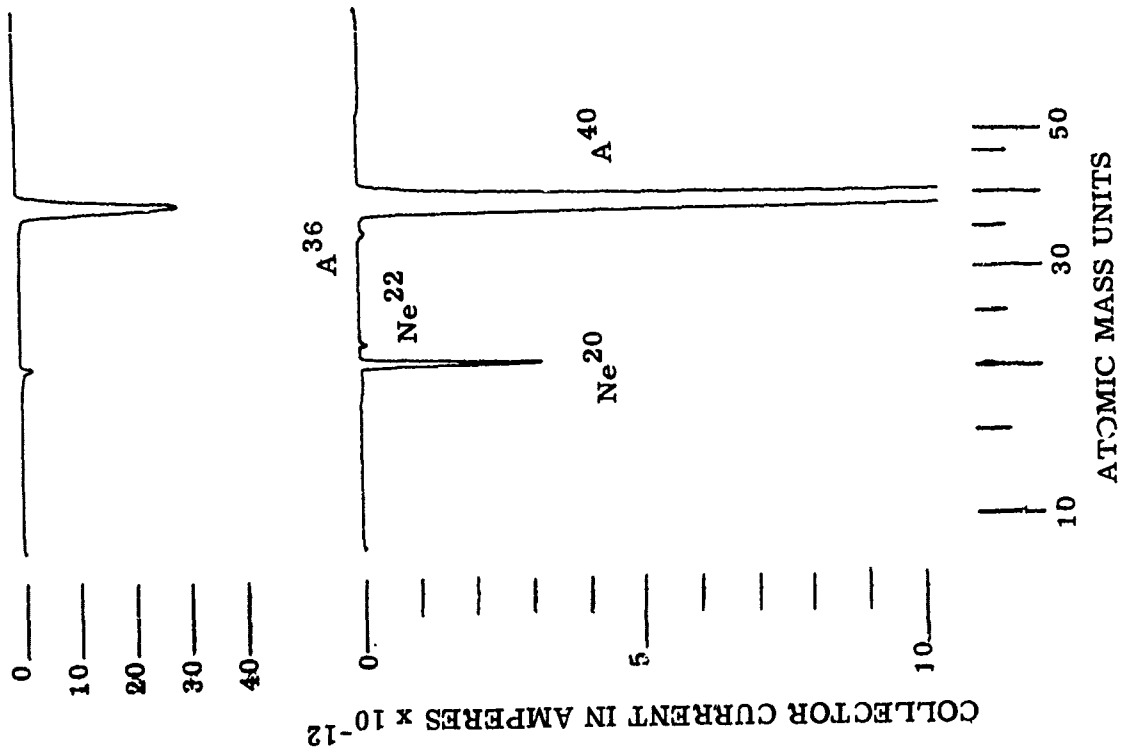


Fig. 29. Enclosed omegatron He peak.

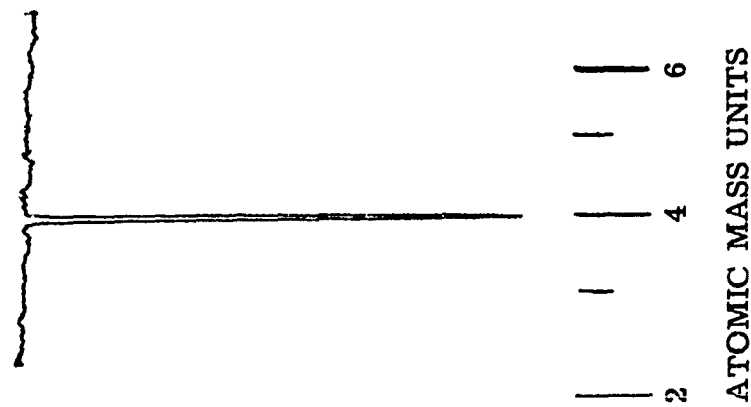


Fig. 30. Enclosed omegatron spectrum at Ne, A, and their isotopes.

TABLE VI

COMPARISON OF EXPERIMENTAL AND PREDICTED RESOLUTIONS

Gas	$\frac{M}{\Delta M}$ [Eq. (A13)]*	$\frac{M}{\Delta M}$ (Fig. 30)
Ne ²⁰	13.9	26
Ne ²²	12.6	31
A ³⁶	7.7	23
A ⁴⁰	6.9	9.3

$$*E_0 = 0.8 \text{ volt/cm}$$

$$P_T = 1.3 \times 10^{-5} \text{ mm Hg}$$

$$B = 4300 \text{ gauss}$$

$$R_0 = 0.25 \text{ cm}$$

The greater magnitude of the observed values of resolution compared with predicted values are probably due to either or a combination of the following causes:

a. Due to the cutoff characteristics evident in Figs. 27 and 28, the spectra of Fig. 30 are in reality only the top portion of the peaks which would be seen in the absence of the cutoff characteristic. Hence, the base-line intercept distance is effectively reduced, yielding apparently higher resolution. One would expect the smaller peaks would show the greatest apparent improvement as evidenced by Ne²² and A³⁶ in Table VI.

b. Since the omegatron electric fields depart considerably from the uniform fields assumed in the derivation which led to Eq. (A13), the ions may gain less energy per cycle from the rf field than the theory indicates, make more revolutions, and have higher resolutions. With the physical configuration of the omegatron, the field at the axis is less than that obtained on the assumption of a uniform field. The same effect is noted in Fig. 31 in which observed resolution of Ne²⁰ as a function of E_0 is plotted and compared with predicted values. While the observed values are everywhere higher, the general shapes of the two curves are similar.

Returning to Fig. 30, we note that the Ne²² peak is about 3.7% of the Ne²⁰ peak and the A³⁶ peak is about 0.4% of the A⁴⁰ peak. The known ratios are approximately 11% and 0.3%, respectively. No explanation is readily available of why argon is approximately correct while neon is in error by a factor of 3.

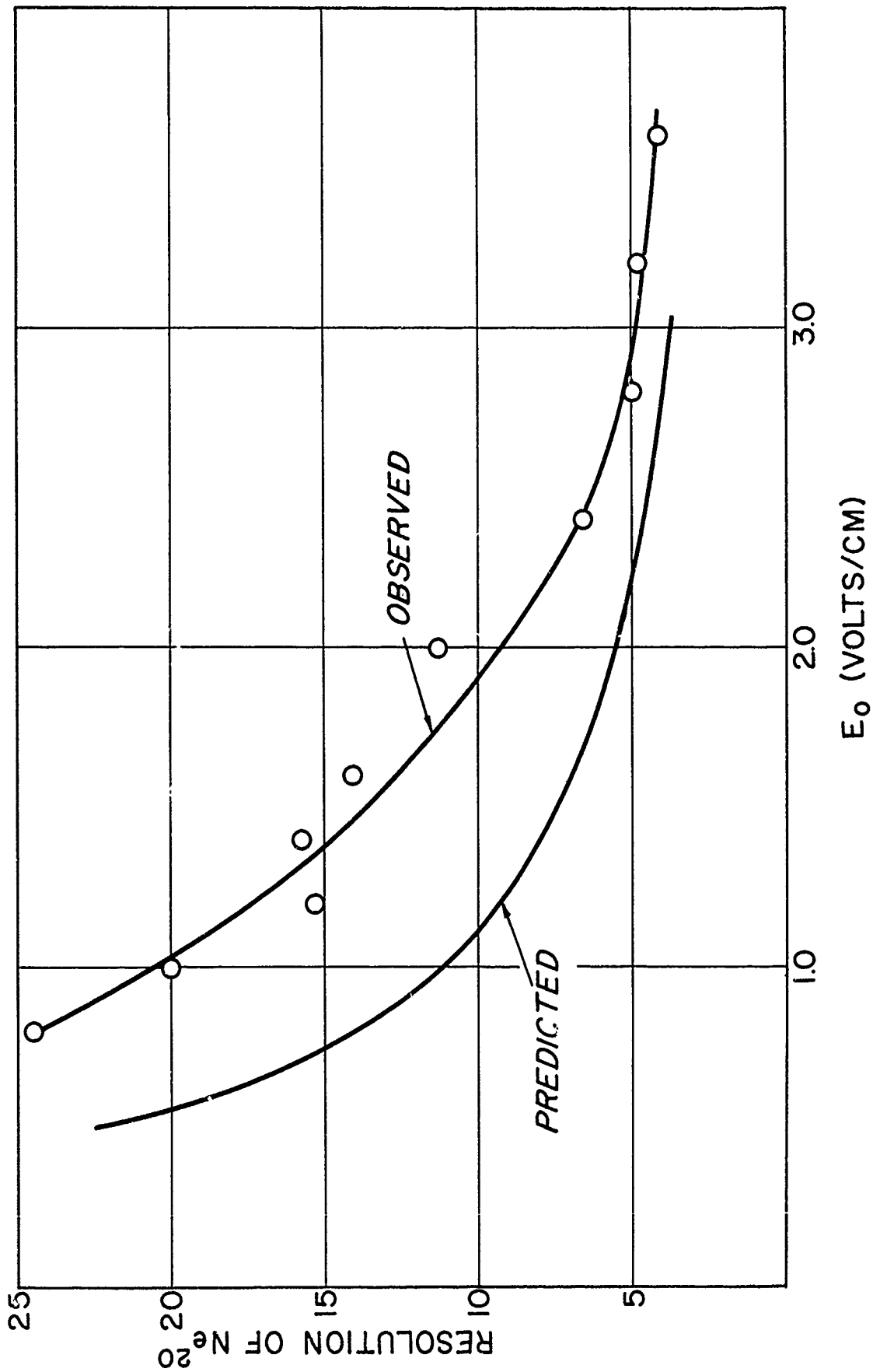


Fig. 31. Omegatron resolution of Ne as a function of E₀.

5.4. CONCLUSIONS

The chief advantage of the omegatron is its theoretical ability to achieve high resolutions, particularly at low mass numbers, with a device of simple construction. From the test results described in the earlier section, the disadvantages may be tabulated as follows:

A. Theoretical

- a. Decrease of resolution with increasing mass number at constant E_0 .
- b. Since the ions are created on the axis of the magnetic field, the pole faces place a limit on reducing the probability of recombination of ambient molecules at the surfaces of the apparatus.

B. Operational

- a. Idealized electric fields are not obtainable with simple electrode structures.
- b. Only the resonant ions are removed. The remainder create radial fields which adversely effect operation.

The "operation" disadvantages give rise to a number of undesirable effects among which are inaccurate abundance ratios as indicated by peak heights, a limitation on the ultimate resolution obtainable and erratic behavior. These all stem directly from the low energies involved (see Table IV), particularly at the higher mass numbers. Since R_0 is fixed by the maximum density and minimum resolution [Eq. (A17)], the only way in which the energy can be increased [Eq. (A18)] is by increasing the flux density, which requires more magnetic material resulting in increased weight.

At these low energies, unsymmetric electric fields inside the omegatron arising from contact potentials seriously disturb the operation. The source of these contact potentials is assumed to be oxides and other contaminants on the omegatron surfaces which give rise to surface work function differences which can result in potential differences of a volt or more. In an attempt to eliminate or reduce this possible source, the unit was induction-heated in a hydrogen atmosphere. Performance was degraded, presumably because the structure did not permit uniform heating and because of additional contamination "boiled" out of the insulators.

At this point, work on the omegatron was discontinued because of the promising performance of the massfilter already described.

It should be noted, however, that the omegatron operates satisfactorily for hydrogen and helium with reasonable magnetic field strengths. This can be attributed to the large ionic energies at the radius of collection (Table IV). The omegatron may therefore have some practical application for use aboard vehicles launched to analyze these light gases.

6. INSTRUMENTATION PACKAGE

The rocket selected by NASA for this work and concurred in by The University of Michigan group is the Nike-Asp. Nose cones from The Cooper Development Company have been received and initial design of the instrument package has been begun.

As mentioned in earlier sections, the presence of large solid surfaces from which ambient gases can be "reflected" to the ionizing region can result in large errors in composition measurement. This occurs since atomic oxygen can recombine to molecular oxygen at the surface. To minimize these effects, the ionizing section is designed to be located about four inches in front of the inlet port, and the intervening cylindrical lens and electron accelerator are composed of fine grids. In this manner, it is hoped to keep the solid angle the ion source sees subtended by solid material in the neighborhood of 10% or less. Thus an approaching particle will have a 90% probability or better of reaching the ionizing volume without first colliding with a solid surface.

Another aspect of grave importance in the design of an instrumentation package is the contribution of gases evolved from the package itself to the measurement in progress. The importance of this aspect has been demonstrated by the long time interval before α ionization gages on Sputnik III reached ambient equilibrium. To minimize this problem, the design of the complete package places the pressurized instrument data cylinder in an evacuated volume. In this manner, the major portion of occluded gases will be removed prior to firing and the errors arising from this source reduced by orders of magnitude.

To eliminate the great volumes of gas and combustion products inherent in explosive separations used in earlier work by this group, a separation technique using the energy released on triggering cocked springs is under development. A satisfactory trigger, activated by burnout of fuse wire, has been developed and a model has been constructed and tested.

Figure 32 is a drawing which illustrates the method of separating the rocket and ejecting the data cylinder from its vacuum chamber. The massenfilter is shown at the forward end of the data cylinder. The pressurized data cylinder contains the FM-FM telemetry transmitter, the filament emission regulator, the driving oscillator, and rectifier for the massenfilter, and the associated amplitude modulator, the electrometer, the monitoring circuits, and the power supplies.

Data transmission is accomplished by means of the illustrated dipole antenna which was selected over self-excitation of the data cylinder itself for two reasons. Self-excitation of the data cylinder would result in the highest electric field strengths at the ends where the massenfilter is located. This is to be avoided, if possible, because of the unavoidable effects on the ion trajectories. In addition, the dipole pattern will be more favorable for transmission to the ground in the normal orientation of the data capsule.

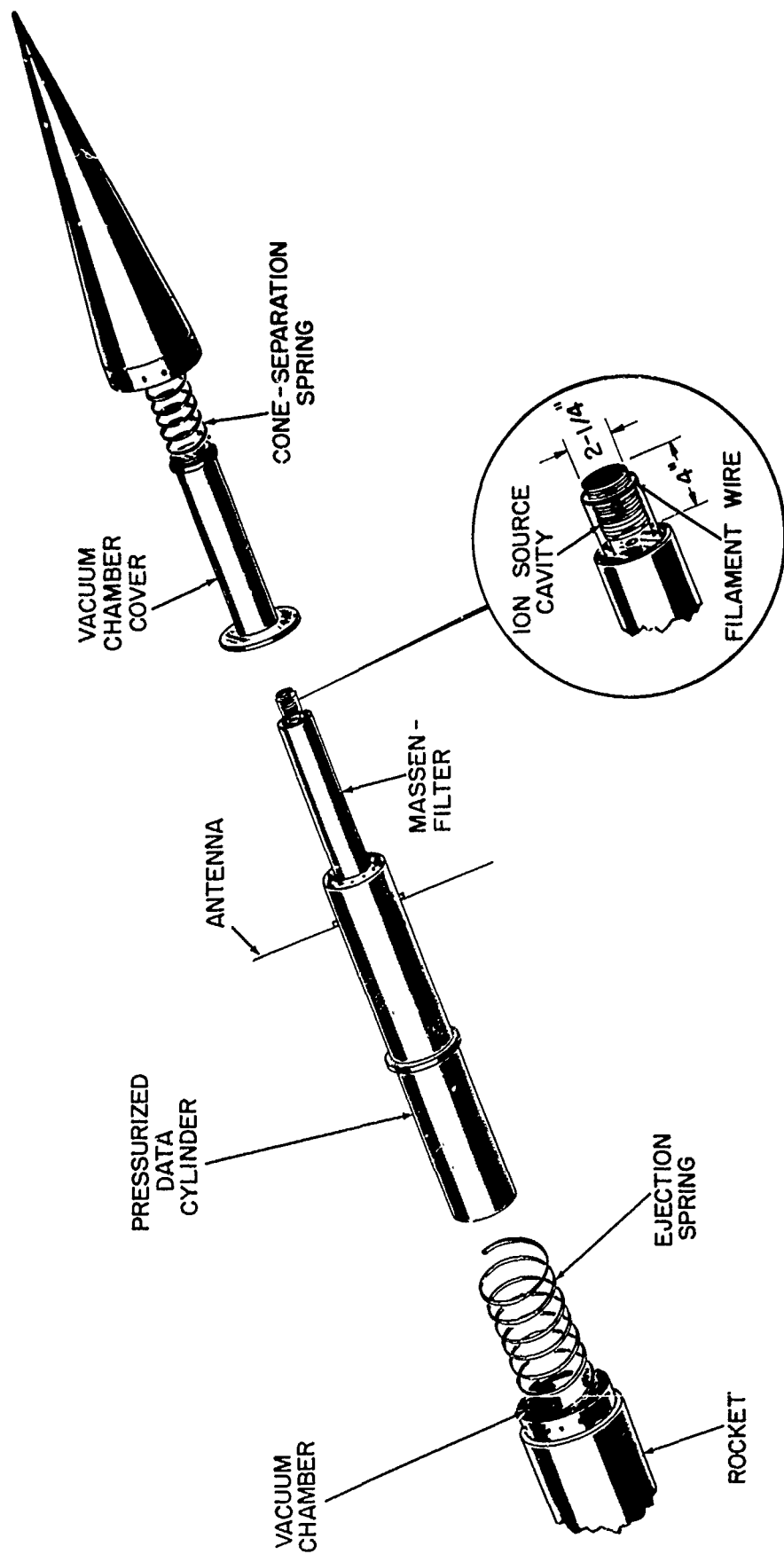


Fig. 32. Data cylinder separation.

7. ELECTRONIC CIRCUITRY

Since the omegatron has been dropped from consideration for this project, a detailed description of the associated electronic circuits, used and planned, does not appear to serve any useful purpose herein. Hence, this section describes only the electronic circuits relating to the massenfilter. In addition, detailed descriptions of standard circuitry such as two d-c electrometers, a balanced output rf amplifier, etc., have been omitted.

7.1. MASSENFILTER DRIVING OSCILLATOR AND RECTIFIER

The rf voltage necessary for operation of the massenfilter is best obtained from a voltage-modulated, push-pull circuit balanced with respect to ground. A pair of d-c voltages of opposite polarity and constant ratio with respect to the rf voltages are required. These are best derived by rectification of the rf voltage and adjusting the ratios by means of voltage dividers.

The laboratory device for deriving these voltages is shown in Fig. 33 and the circuit diagram is given in Fig. 34. The rf generator is simply a tuned-grid, tuned-plate, push-pull oscillator. For laboratory use, a mass sweep derived from voltage modulation is accomplished by sweeping the B+ voltage. The capacity of the massenfilter rods forms part of the tank circuit. Tuning of the tank is accomplished by use of the variable 150-mmF condenser and balance with respect to ground is accomplished with the two 50-mmF condensers from each end of the tank to ground. The d-c voltages are derived by rectifying the rf voltage at each end of the tank and impressed on the respective rods pairs through a pair of isolating 2.5-mH chokes. The ratio of d-c to rf voltages is adjustable by means of the 200-K potentiometers seen in Fig. 34. This unit is seen as part of the laboratory test setup shown in Fig. 35.

For flight use, a crystal-controlled, master oscillator, amplitude-modulated, power amplifier of miniaturized construction is under active development.

7.2 EMISSION REGULATOR

Ambient conditions, particularly at the lower altitudes, will have large effects on the emission characteristics of whatever filament is selected as the massenfilter electron source. Hence, some means of regulating the emission must be provided. Transistorized emission regulators have been described in the literature,^{17,18} and a unit operating on these principles has been constructed with minor design modifications to adapt it to the application. The circuit diagram is given in Fig. 36 and the laboratory unit is shown in Fig. 37 together with its associated test equipment.

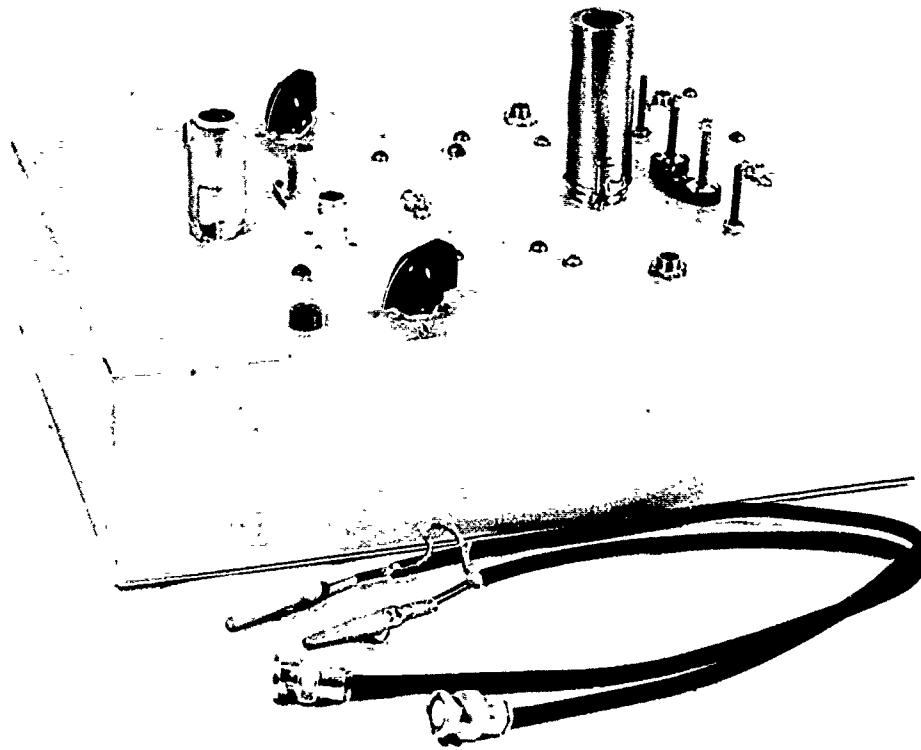


Fig. 33. Massenfilter oscillator and rectifier.

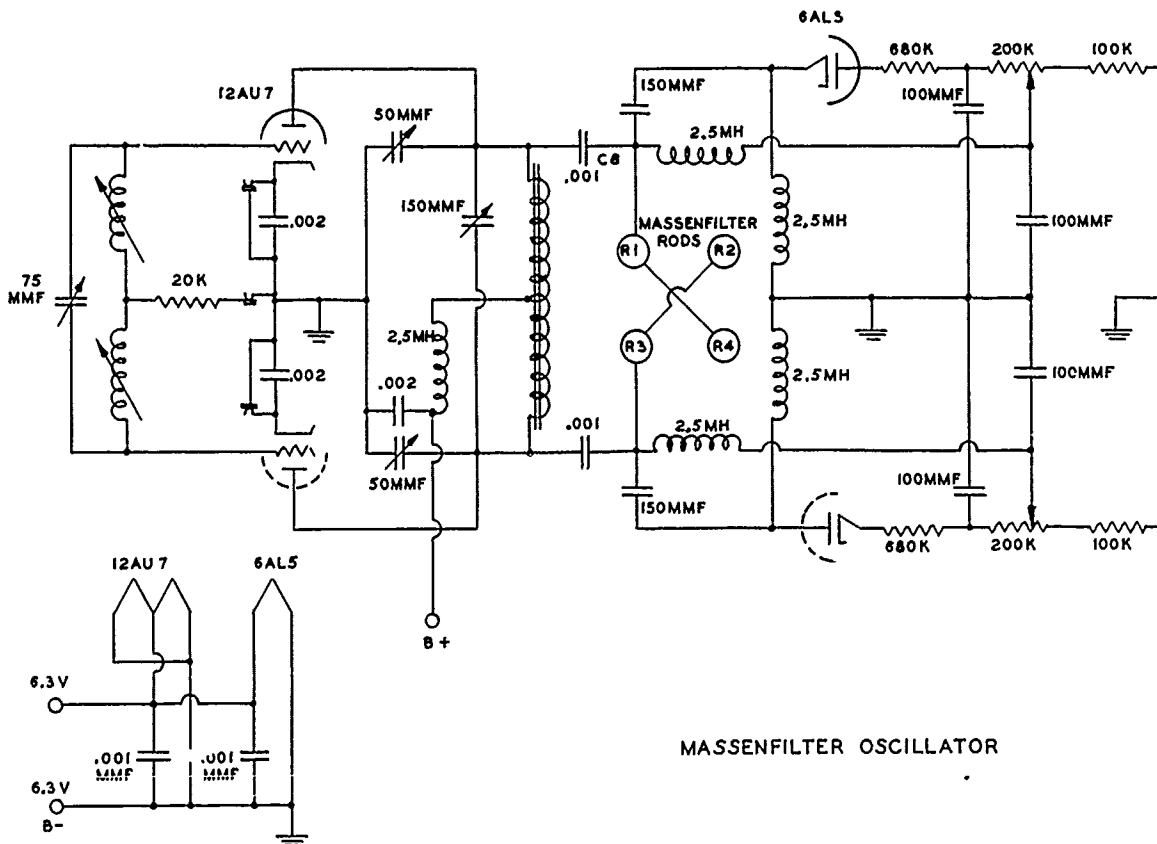


Fig. 34. Circuit diagram: Massenfilter oscillator and rectifier.

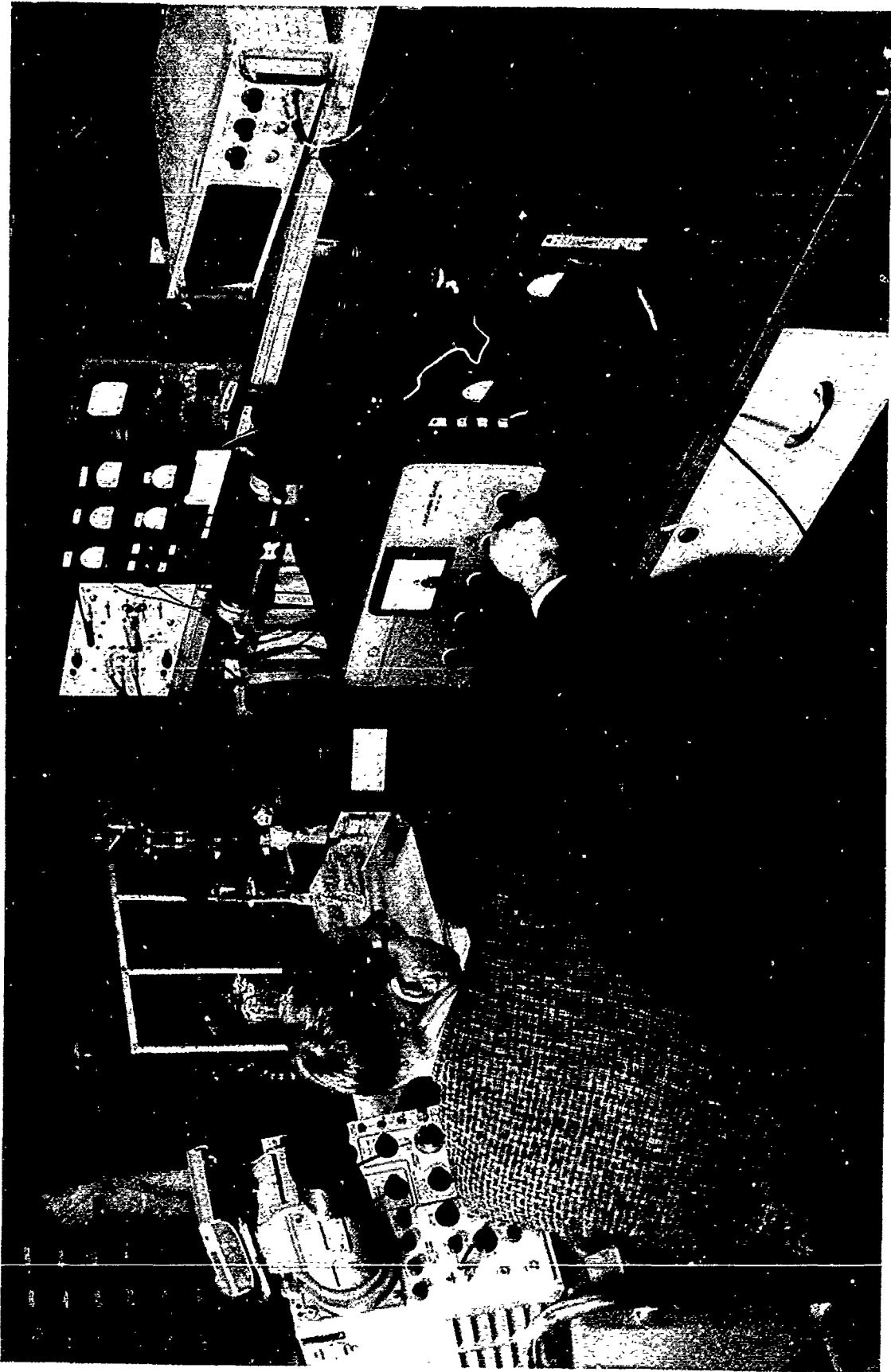
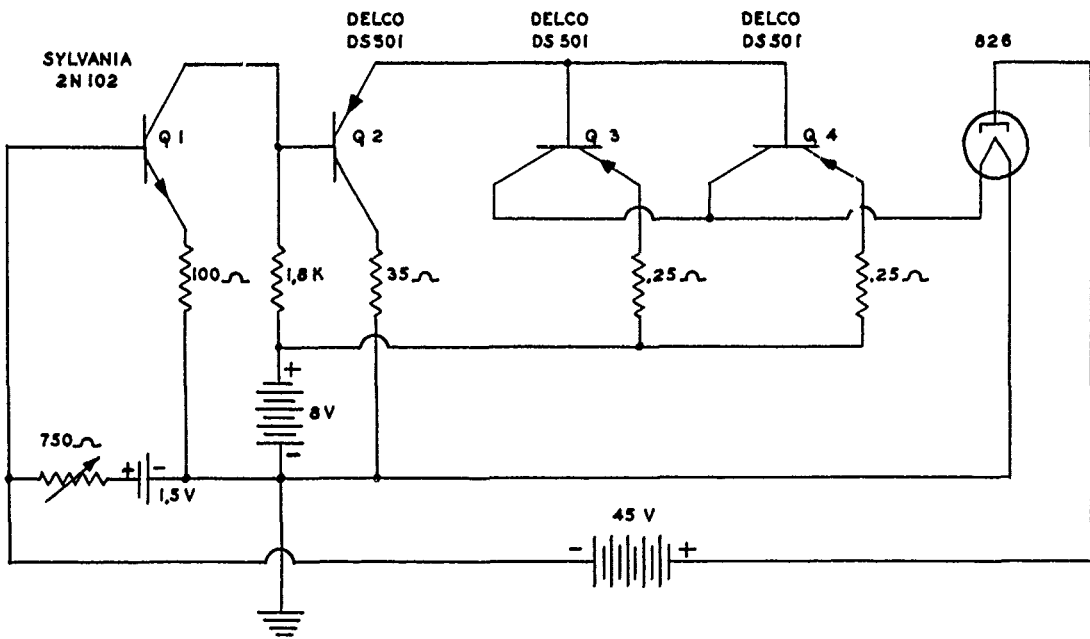


Fig. 35. Laboratory test setup.



EMISSION CURRENT REGULATOR

Fig. 36. Circuit diagram: emission regulator.

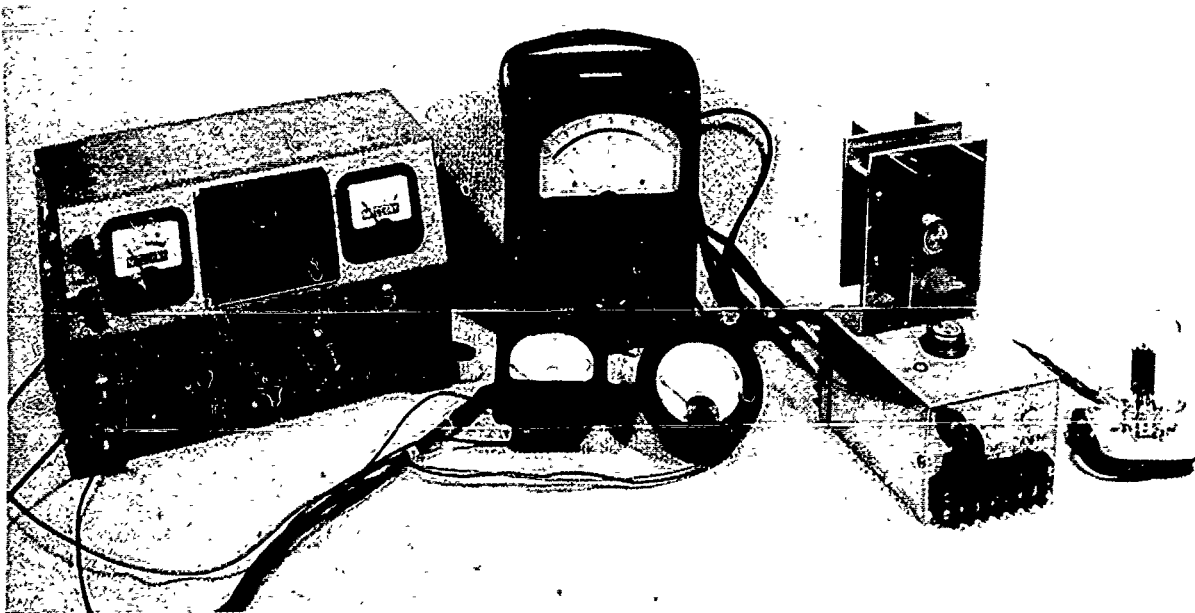


Fig. 37. Emission regulator.

The base current input of Q_1 is the difference between the emission current of the regulated filament and the current produced by the reference battery in the adjustable emission regulating resistance. If the emission current is smaller than the reference current, Q_1 will be in conduction and amplify the difference current which is then the input to Q_2 . Transistor Q_2 is a grounded collector used to convert the amplified output of Q_1 to a low impedance to drive the parallel current regulators, Q_3 and Q_4 . These latter transistors in effect act as controllable variable resistors in the filament circuit. As long as emission current is less than the adjusted reference current, the current regulating transistors are in full conduction, delivering maximum heating power to the filament. Operation stabilizes at the filament heating current which produces the reference emission current.

As is evident from Figs. 36 and 37, initial testing of the circuit was accomplished using a standard 826 power rectifier as a dummy load. Testing of the circuit resulted in an emission current which remained within 1% of its adjusted value over a plate voltage range of from 22-1/2 to 100 volts and over a filament supply battery range of from 4 to 12 volts. The circuit operation is stable throughout.

While this circuit is suitable for flight use, it is inefficient since a large fraction of the power drawn from the filament supply battery is expended in the variable resistance by which the regulating transistors may be represented. In addition to being inefficient, the power dissipated in the transistors requires the heat sink seen in Fig. 37 to prevent a temperature rise sufficient to result in runaway operation. Accordingly, a regulation circuit which operates the filament control transistors as switches is under development. In this manner, power dissipation in the transistors is at the minimum possible value. Regulation is accomplished by maintaining a constant switching rate but varying the on-off duty cycle as required. If the switching rate is sufficiently beyond the temperature time constant of the filament, no significant modulation will result. Any residual modulation will be at a frequency beyond the response limits of the massenfilter electrometer circuit. Although the initial version of the circuit is under test, the results are of only a preliminary nature at this writing.

7.3. TELEMETRY

The standard IRIG FM-FM telemetry system has been chosen as best adapted to the requirements of the project. If possible, a commercial transmitter and ground system will be purchased. Toward this end, data on such systems and related components have been obtained from several companies. Actual selection and placement of orders, however, await further funding.

A visit to Wallops Island in June, 1959, disclosed the existence of a partial IRIG ground station there at that time and the expectancy of installing a permanent IRIG telemeter receiving station in the indefinite future. It is proposed to use the Wallops Island facilities as a backup to the project sta-

tion. In any event, a project station is necessary for tests of the overall system, including the rf link and tape recorder, prior to shipment. In addition, playback of flight data from magnetic tape requires the use of the entire ground station except for the receiver and antenna. Finally, a complete system is necessary if the experiment is to be synoptic.

The frequency approved for Wallops Island in June was 240.2 Mc with additional requests for 244.3 Mc and 256.2 Mc. Final frequency selection will be made about the same time orders are placed.

8. VACUUM EQUIPMENT

In support of the omegatron and massenfilter test and development programs, a total of four high-vacuum systems have been constructed. Two of these are all-glass systems, one of which is portable. These are shown in Figs. 38 and 39 and a closeup of one appears in Fig. 40 to show the mercury shut-off valves and the liquid nitrogen traps. In addition, a completely dry, stainless-steel system has been purchased from Varian Associates and assembled as shown in Fig. 41. Prepumping is accomplished by the activated charcoal trap chilled by liquid nitrogen, at the bottom of the system. Upon attaining a pressure of about 20 microns, the trap is shut off or pinched off the system and high vacua obtained with the Vac-Ion pump at the top. An ionization gage is mounted from one flange of the crossed tubulation and the instrument to be tested will be mounted on the remaining flange shown pinched off in Fig. 41. Completely satisfactory operation has not yet been achieved due to leaks. Elimination of such leaks is in progress.

Finally, a high-capacity oil diffusion pump has been fitted with demountable tubulation to aid in rapid testing of design changes in the massenfilter ion source.

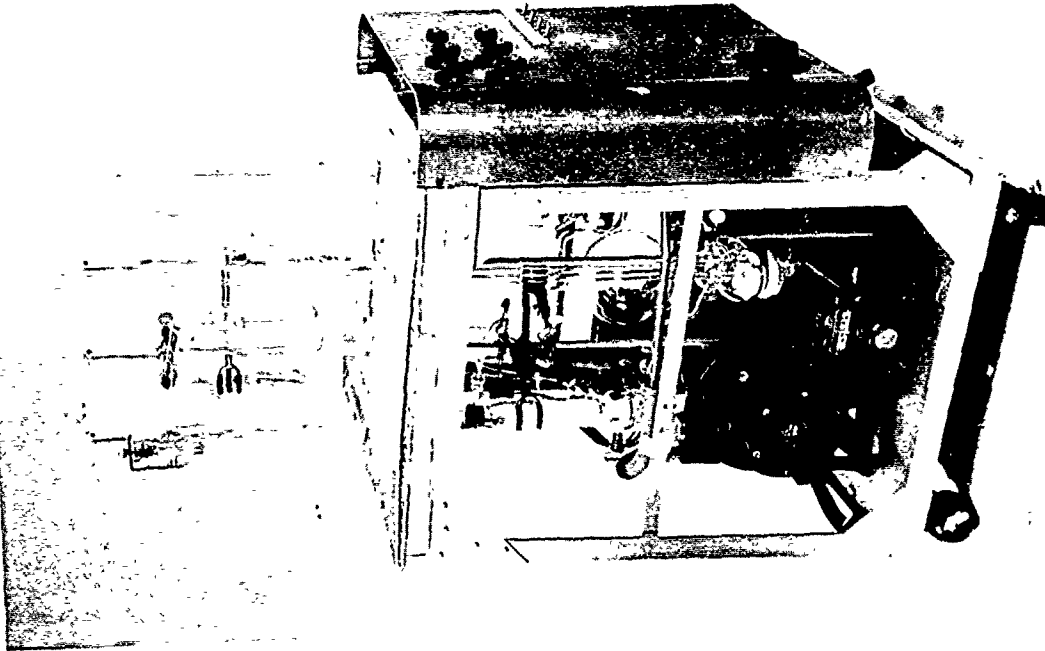


Fig. 39. Portable glass vacuum system.

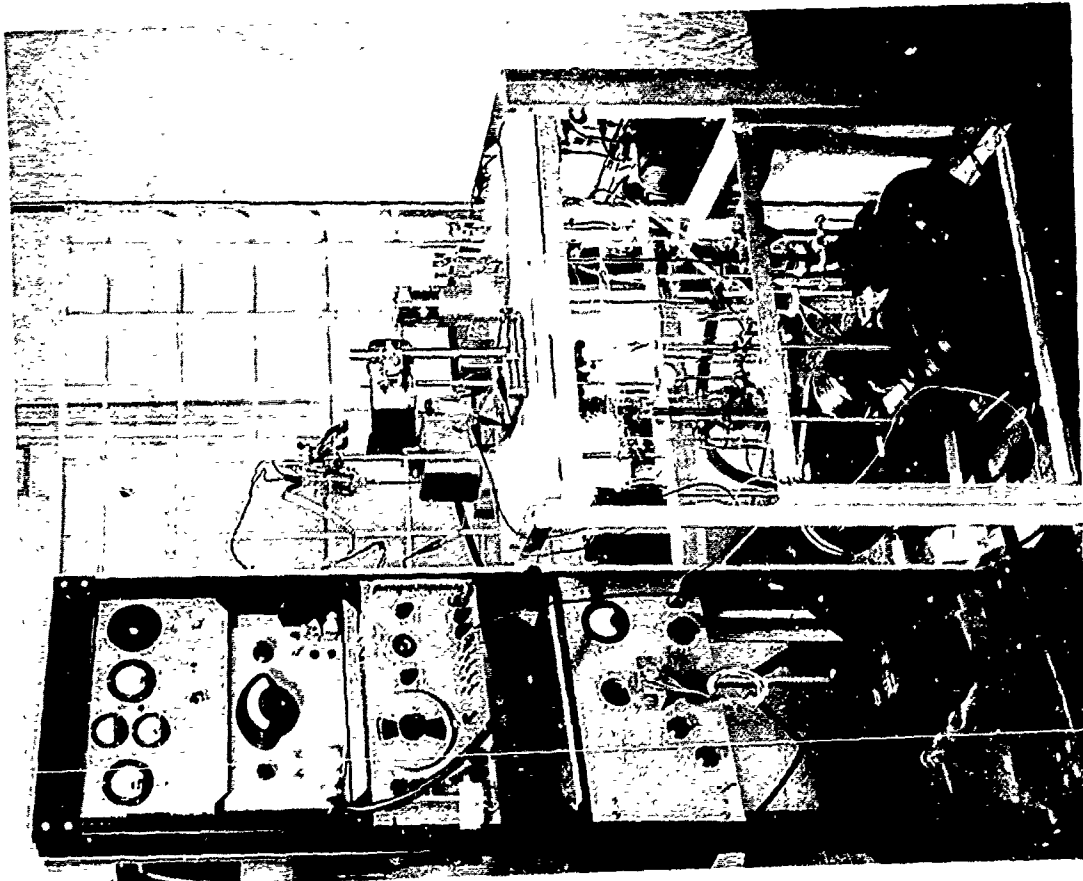


Fig. 38. Glass vacuum system.

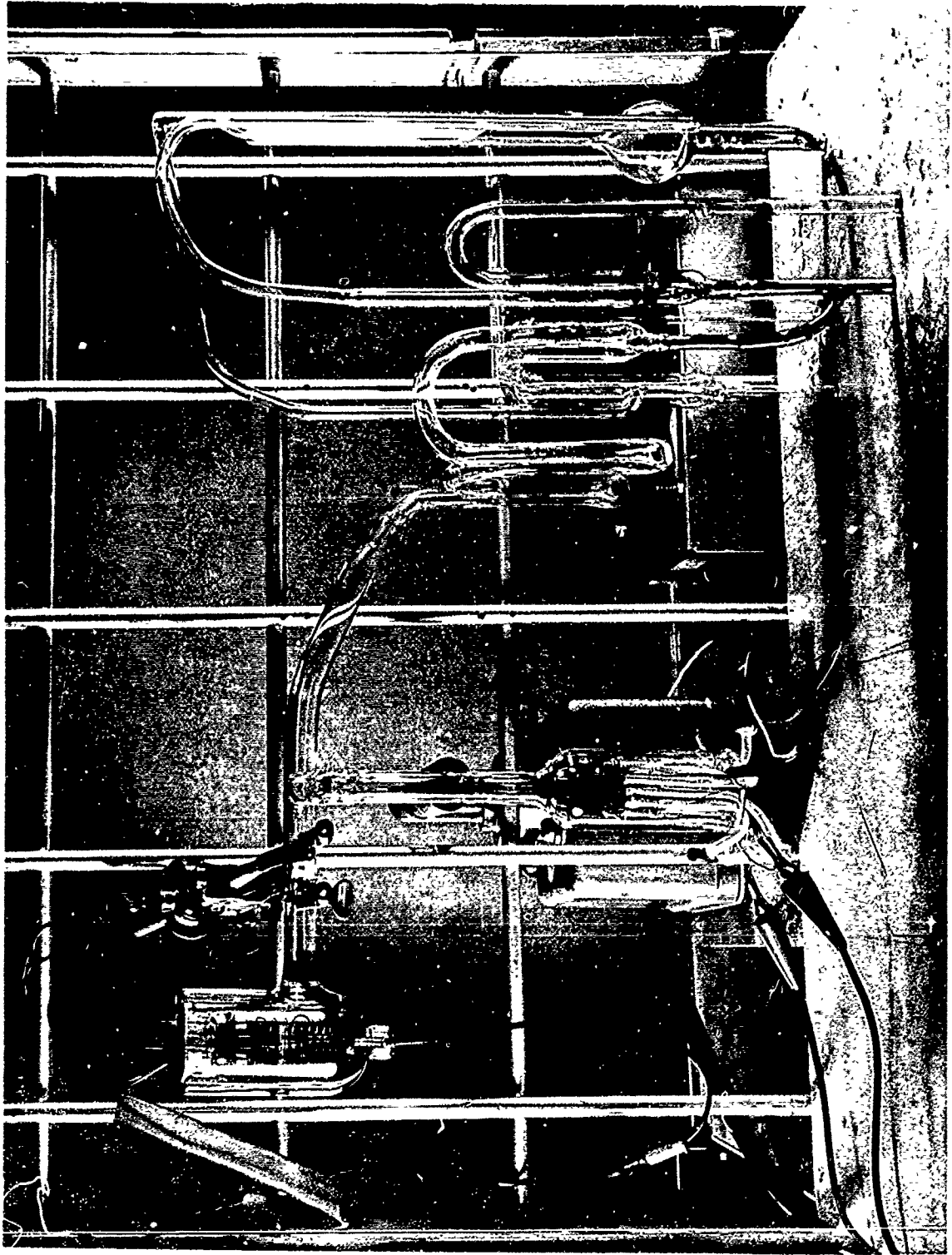


Fig. 40. Closeup of glass vacuum system.

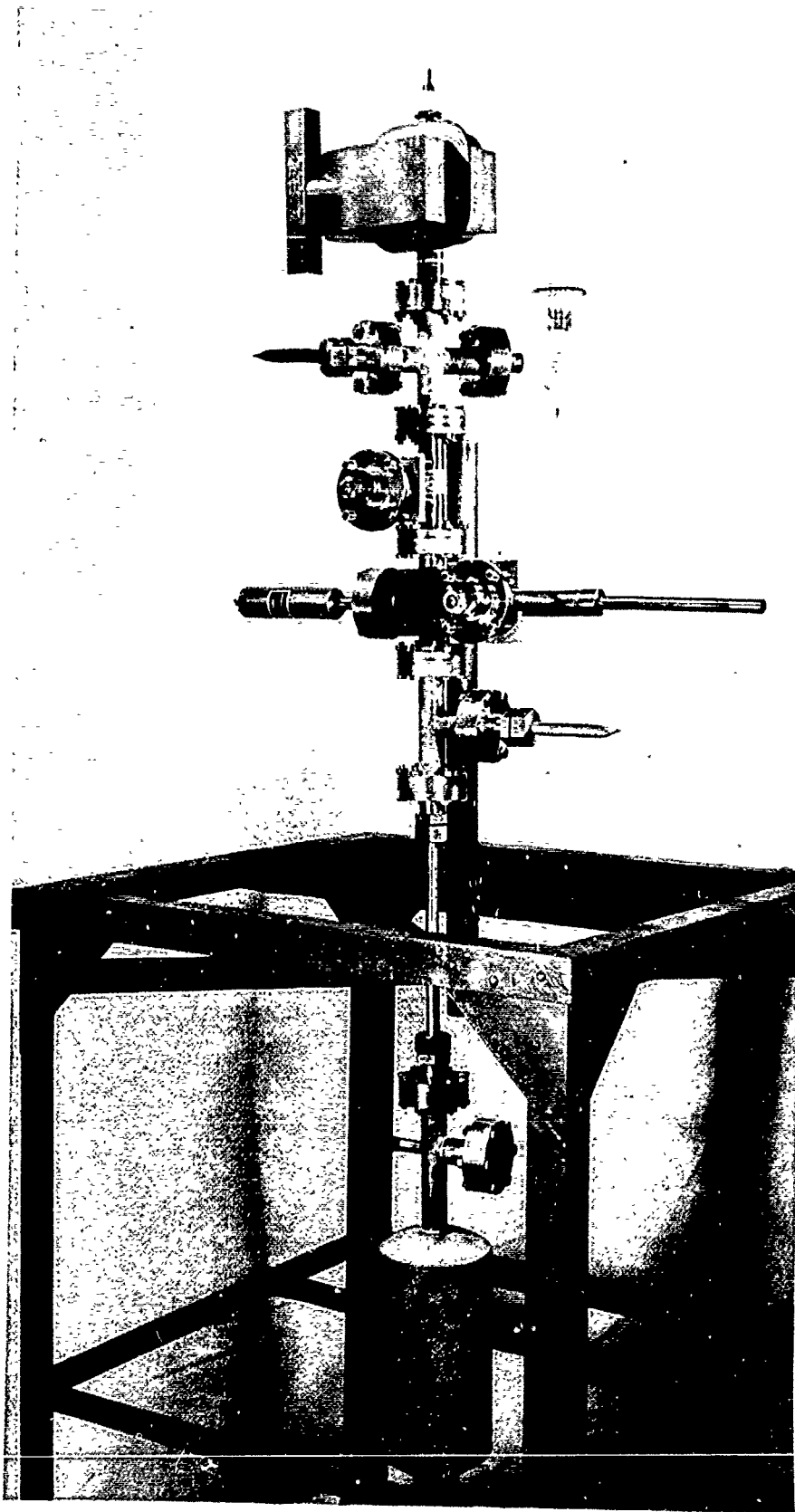


Fig. 41. Stainless-steel vacuum system.

9. FUTURE PROGRAM

Sufficient data indicating satisfactory operation and reliability of the massenfilter have been obtained to commit the program to its use. Flight design will differ from the prototype only in detail and this effort is underway. This design will be completed and three units will be built and checked. The supporting electronics, already underway, will be packaged for flight use. The major remaining items to be designed and developed are the flight electrometers and the in-flight monitoring and calibration circuitry. The largest item of equipment to be purchased is the telemetry system. This equipment will be purchased with first-year money which is temporarily being diverted to project operating expenses in anticipation of funds to carry out the second year's work.

In all, three complete airborne units will be built initially for a series of firings tentatively scheduled for the second quarter of 1960 at Wallops Island. The exact relative firing times as well as the number of those actually fired will be determined by the degree of success enjoyed on the initial rounds.

The major problem which is anticipated for final adaptation to synoptic use is the manner in which data will be correlated with altitude in the absence of tracking facilities such as are located at Wallops Island. Possibilities include a simple single station DOVAP-ballistic camera tracker or the relation of a small range of the observed data to ambient conditions, either known or independently measured, to obtain a single altitude-time point from which the remainder of the trajectory can be computed. This latter assumes data symmetry will yield peak time. A similar method has been successfully used in the falling sphere experiment pioneered by this group. Very little effort has been available for solution of this problem, however, in the course of the initial work of sensor development, and it has been necessarily delayed for the future program.

10. ACKNOWLEDGMENTS

We are indebted to the NASA for financial support of the work reported herein as well as the valuable comments and suggestions which have been made in the course of discussions. In particular, the cooperation of Mr. Herman LaGow and Mr. Maurice Dubin has been highly valued. Mrs. Edith Meadows' discussions on the Bennett tube and mass spectrometry of the upper atmosphere in general have been very helpful.

The cooperation of Dr. H. C. Corben and his staff at the Ramo-Wooldridge Corporation in discussions on the applications of the stability regions predicted by the Mathieu equation is gratefully acknowledged. Finally, the analytical assistance of Professor Edward O. Gilbert, currently at the Space Technology Laboratories on leave from the Department of Aeronautical and Astronautical Engineering, has been genuinely appreciated.

APPENDIX

OMEGATRON: PRINCIPLE OF OPERATION

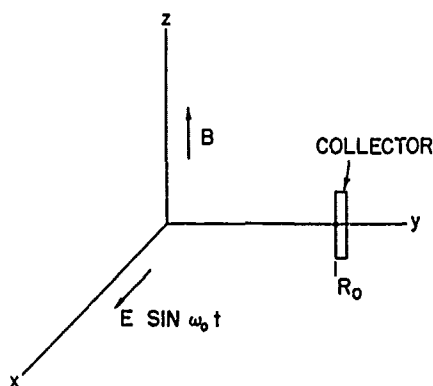
Analysis of the operating principles of the omegatron has been covered in the literature.⁹⁻¹⁵ For the convenience of the reader, the following presents the pertinent equations and the method by which they are obtained.

A. EQUATIONS

The differential equations of motion of an ion in crossed rf electric and magnetic fields (Fig. 42) are

$$m \frac{d^2x}{dt^2} = eE \sin \omega_0 t + eB \frac{dy}{dt} \quad (A1)$$

$$m \frac{d^2y}{dt^2} = -eB \frac{dx}{dt} \quad (A2)$$



where:

- m = ion mass in grams,
- x, y = coordinate distances in cm,
- e = electronic charge in emu,
- E = electric field strength in emu units, and
- B = magnetic flux density in gauss.

Fig. 42. Omegatron field coordinates.

Making the substitutions

$$\omega = eB/m \quad (A3)$$

$$\alpha = eE/m \quad (A4)$$

and using initial conditions (since the ionizing electron beam is confined to the Z axis),

$$y = 0, \quad x = 0, \quad \frac{dx}{dt} = u, \quad \frac{dy}{dt} = v, \quad \omega_0 t = \phi$$

Simultaneous solution of (A1) and (A2) yields

$$\begin{aligned}
x + iy &= \frac{i\vec{V}}{\omega} \left[e^{-i\omega(t-\phi/\omega_0)} - 1 \right] - i \frac{\alpha}{\omega_0^2 - \omega^2} \left[\frac{\omega}{\omega_0} \cos \omega_0 t - i \sin \omega_0 t \right] \\
&+ i \frac{\alpha}{\omega_0^2 - \omega^2} \left[\frac{\omega_0}{\omega} \cos \phi - i \sin \phi \right] e^{-i\omega(t-\phi/\omega_0)} - i \frac{\alpha}{\omega \omega_0} \cos \phi \quad (A5)
\end{aligned}$$

where $\vec{V} = u + iv$.

Finding the limit of (A5) as $\omega_0 \rightarrow \omega$, substituting $\epsilon = \omega - \omega_0$, neglecting the first term due to initial velocity (to be treated later), and finally assuming $\omega_0 \cong \omega$ and $\epsilon \ll \omega_0$, one can obtain, in the vicinity of resonance,

$$\vec{r} = x + iy \cong \frac{i\alpha}{2\omega_0\epsilon} e^{-i\omega_0 t} \left[1 - e^{-i\epsilon(t-\phi/\omega_0)} \right] \quad (A6)$$

In the immediate vicinity of resonance, Ref. 12 shows that, after a few revolutions, the position of an ion is relatively independent of the phase angle of the electric field at its creation. Setting $\phi = 0$, (A6) can be further simplified to

$$r = \frac{E}{B\epsilon} \sin \frac{\epsilon t}{2} \quad (A7)$$

At a frequency slightly off resonance, the amplitude of r will oscillate at a frequency of $\epsilon/4\pi$ cps and will never exceed $E/B\epsilon$. At resonance, the limit of (A7) as $\epsilon \rightarrow 0$ yields the expression

$$r = \frac{Et}{2B} \quad (A8)$$

Thus one can see that the resonant ionic path is an Archimedes' spiral and the radius increases with time at a uniform rate. If a collector is located R_0 from the axis, charged particles will never reach it if, from (A7),

$$R_0 > \frac{E}{B\epsilon} \quad (A9)$$

Thus, there is a critical value

$$\epsilon' = \frac{E}{R_0 B} \quad (A10)$$

for which ions just reach the collector. Defining resolution as

$$\frac{M}{\Delta M} = \frac{\omega}{2\epsilon'} \quad (A11)$$

(center frequency/frequency width of base), then

$$\frac{M}{\Delta M} = \frac{\omega R_0 B}{2E} = \frac{R_0 B^2 e}{2E m} \quad (A12)$$

$$= 4.8 \times 10^{-5} \frac{R_0 B^2}{E_0 M} \text{ in practical units} \quad (A13)$$

where, in (A13)

B = magnetic flux density in gauss,
 R_0 = collector radius in cm,
 E_0 = peak electric field gradient in volts/cm, and
M = atomic mass units.

It can be easily shown that the length of an Archimedes' spiral is equal to the number of revolutions multiplied by the circumference of the turn of average radius. Thus the path length of the resonant ion at collection is

$$L = \pi n R_0 \quad (A14)$$

where n is the number of turns prior to collection. Now

$$\omega = 2\pi f = \frac{2\pi n}{t} = \frac{eB}{m} \quad (A15)$$

and

$$\pi n = \frac{eBt}{2m} = \frac{eB}{2m} \frac{2BR_0}{E} = \frac{eB^2 R_0}{Em} = 2 \frac{M}{\Delta M} \quad (A16)$$

using (A8) and (A12). Substituting (A16) into (A14), we have

$$L = 2R_0 \frac{M}{\Delta M} \quad (A17)$$

The energy of the resonant ion at collection is given by

$$W = \frac{1}{2} mv^2 = \frac{1}{2} m\omega^2 R_0^2 = \frac{1}{2} mR_0^2 \frac{e^2 B^2}{m^2} = \frac{1}{2m} (eBR_0)^2 \quad (A18)$$

B. EFFECT OF INITIAL VELOCITY

Equation (A5) shows that an initial velocity, \vec{V} , of an ion superimposes a circular motion upon the Archimedes' spiral arising from the action of the elec-

tric rf field.* The circle is tangent to the velocity vector \vec{V} at the origin, has an angular velocity equal to ω , the ion resonant frequency, and a radius of $|V|/\omega$. An analysis of the effects of the initial velocity shows that the resolution is modified since the number of turns prior to collection is changed. In addition, the maximum orbital dimensions are also changed. If, as indicated in Fig. 42, a collector parallel to the z-axis is placed along the positive y-axis at R_0 , the effects of \vec{V} are given in Table VII for several directions of the vector velocity.

TABLE VII
EFFECT OF INITIAL VELOCITY

Direction of \vec{V}	Direction of Center of Circle	Effective $M/\Delta M$	Maximum Orbital Dimensions	
			Along -y axis	Along $\pm x$ axis
$\vec{V} = 0$	0	$\frac{R_0 B^2 e}{2mE}$	R_0	R_0
+x	-y	$\frac{R_0 B^2 e}{2mE}$	$R_0 + \frac{2v}{\omega}$	$R_0 + \frac{v}{\omega}$
-x	+y	$\frac{(R_0 - \frac{2v}{\omega}) B^2 e}{2mE}$	$R_0 - \frac{2v}{\omega}$	$R_0 - \frac{v}{\omega}$
$\pm y$	$\pm x$	$\frac{R_0 B^2 e}{2mE} \left[\frac{R_0}{\frac{v}{\omega} + \sqrt{(\frac{v}{\omega})^2 + R_0^2}} \right]$	$\sqrt{R_0^2 + (\frac{v}{\omega})^2}$	$\frac{v}{\omega} + \sqrt{R_0^2 + (\frac{v}{\omega})^2}$

The effective values of resolution above are based on those ions which are created at the phase angle which results in the fewest number of revolutions while the maximum orbital dimensions are independent of phase angle. The practical effects of an initial velocity are to reduce the effective resolution, depending on the vector direction, and to require electrode spacings which allow the ion to reach the collector before its orbit carries it into one of the surfaces.

*Initial velocity of the ion in our application arises from thermal energy and the relative motion of the rocket with respect to the ambient atmosphere.

C. EFFECTS OF A SUPERIMPOSED D-C FIELD

The path of an ion in crossed d-c electric and magnetic fields is known to be a cycloid and can be expressed by the parametric equations:

$$y = -\frac{\alpha'}{\omega^2} (\omega t - \sin \omega t) \quad (C1)$$

$$x = \frac{\alpha'}{\omega^2} (1 - \cos \omega t) \quad (C2)$$

where

$$\begin{aligned} \alpha' &= eE'/m, \\ E' &= \text{d-c electric field gradient, and} \\ \omega &= eB/m. \end{aligned}$$

From (C1) and (C2) it can be noted that the x-axis excursion of the ion is limited between the values zero and $2\alpha'/\omega^2$, while it proceeds down the negative y-axis at an averaged velocity given by

$$\frac{\alpha'}{\omega} = \frac{eE'}{m} \frac{m}{eB} = \frac{E'}{B} \quad (C3)$$

In Ref. 12, C. E. Berry suggests that this effect can be used to sweep continuously all nonresonant ions from the analyzing volume due to their drift down the negative y-axis away from the collector. Comparing (C3) with (A8), we note that when $E'/B = E/2B$, the resonant ion will not gain or lose any distance toward the collector in its orbital path. Hence, for collection, $E' < E/2$ must be satisfied. When E' is adjusted to $E/4$, for example, the ratio of the negative to positive y-axis orbital radii is 3:1. Hence, in this case, the effective R_0 is twice the distance of collector from beam axis.

REFERENCES

1. Minzner, R. A., and Ripley, W. S., "The ARDC Model Atmosphere, 1956," Air Force Surveys in Geophysics, No. 86, 1956.
2. Whitney, C. A., "The Structure of the High Atmosphere II. A Conduction Model," Nat. Acad. Sci. IGY Satellite Report Series, No. 8, pp. 115-121, 1959.
3. Chapman, S., "The Earth in the Sun's Atmosphere," Sci. Amer., 201, No. 4, 64-71 (1959).
4. Nicolet, M., "High Atmosphere Densities," Science, 127, No. 3310, 1317-1320 (1958).
5. Meadows, E. B., and Townsend, J. W., "Diffusive Separation in the Winter Nighttime Arctic Upper Atmosphere 112 to 150 Km.," Nat. Acad. Sci. IGY Rocket Report Series, No. 1, pp. 107-119. Also a private communication.
6. Paul, W., Reinhard, H. P., and van Zahn, U., "Das elektrische Massenfilter als Massenspektrometer und Isotopentrenner," Zeitschrift für Physik, 152, 143-182 (1958).
7. Dayton, I. E., Shoemaker, F. C., and Mozley, R. F., "The Measurement of Two-Dimensional Fields. Part II: Study of a Quadrupole Magnet," Rev. Sci. Instr., 25, No. 5, 485-489 (1954).
8. Stoker, J. J., Nonlinear Vibrations, Interscience Publishers, Inc., N. Y., 1950.
9. Hipple, J. A., Sommer, H., and Thomas, H. A., "A Precise Method of Determining the Faraday by Magnetic Resonance," Phys. Rev., 76, No. 12, 1877-1878 (1949).
10. Sommer, H., and Thomas, H. A., "Detection of Magnetic Resonance by Ion Resonance Absorption," Phys. Rev., 78, No. 6, 806 (1950).
11. Sommer, H., Thomas, H. A., and Hipple, J. A., "The Measurement of e/m by Cyclotron Resonance," Phys. Rev., 82, No. 5, 697-702 (1951).
12. Berry, C. E., "Ion Trajectories in the Omegatron," J. Appl. Phys., 25, 28-31 (1954).
13. Alpert, D., and Buritz, R. S., "Ultra-High Vacuum II. Limiting Factors on the Attainment of Very Low Pressures," J. Appl. Phys., 25, 202-209 (1954).

14. Woodford, H. J., and Gardner, J. H., "Method for Eliminating Omegatron Radial Field Errors or for Direct Measurement of Mass Ratios," Rev. Sci. Instr., 27, 378-381 (1956).
15. Wagener, J. S., and Marth, P. T., "Analysis of Gases at Very Low Pressures by Using the Omegatron Spectrometer," J. Appl. Phys., 28, 1027-1030 (1957).
16. Meadows, E. B., and Townsend, J. W., "Neutral Gas Composition of the Upper Atmosphere by a Rocket-Borne Mass Spectrometer," J. Geophys. Res., 61, 576-577 (1956).
17. Holmes, J. C., "Emission Current Regulator for Rocket-Borne Radio-Frequency Mass Spectrometer," Rev. Sci. Instr., 28, No. 4, 290-291 (1957).
18. Benton, H. B., "Small Lightweight Ionization Gauge Control Circuit," Rev. Sci. Instr., 30, No. 10, 887-888 (1959).